RESEARCH ARTICLE | AUGUST 25 2025

# Influence of hull-propeller-rudder interaction on the self-propulsion of wind-assisted ships

Saeed Hosseinzadeh 🗷 💿 ; Dominic Hudson 💿 ; Stephen R. Turnock 💿 ; Martyn Prince 💿 ; Joseph Banks 💿



Physics of Fluids 37, 087216 (2025) https://doi.org/10.1063/5.0281083





# Articles You May Be Interested In

Experimental and computational study of hull-propeller-rudder interaction for steady turning circles

Physics of Fluids (December 2021)

Hull-propeller-rudder interaction of the JBC ship model

AIP Conf. Proc. (November 2020)

Effect of stern hull shape on turning circle of ships

AIP Conf. Proc. (June 2012)



**Physics of Fluids** 

**Special Topics Open** for Submissions

**Learn More** 



# Influence of hull-propeller-rudder interaction on the self-propulsion of wind-assisted ships

Cite as: Phys. Fluids **37**, 087216 (2025); doi: 10.1063/5.0281083 Submitted: 16 May 2025 · Accepted: 1 August 2025 · Published Online: 25 August 2025

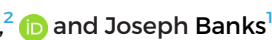








Saeed Hosseinzadeh, la 🕞 Dominic Hudson, 🕞 Stephen R. Turnock, 🕞 Martyn Prince, 🗀 and Joseph Banks 🕞





# **AFFILIATIONS**

 $^1$ Faculty of Engineering and Physical Sciences, University of Southampton, Burgess Road, Southampton SO16 7QF, United Kingdom  $^2$ Wolfson Unit for Marine Technology and Industrial Aerodynamics, University of Southampton, Burgess Road, Southampton SO16 7QF, United Kingdom

#### **ABSTRACT**

Wind-assisted propulsion systems represent one of the most promising technologies for decreasing greenhouse gas emissions in shipping, offering significant potential to reduce fuel consumption. There is a complex interaction between the forces and moments generated by the wind assist device and the hydrodynamic performance of the ship's hull, propeller, and rudder. An experimental investigation was conducted in the 138 m Boldrewood towing tank using a 1/61 scale geosim of a single-screw containership hull. Hull, propeller, and rudder forces were measured through resistance, non-propelled, and self-propelled captive tests at a full-scale representative service speed of 18 knots. Tests covered typical wind assist conditions using four offloaded propeller conditions, simulating partial thrust from wind of 10%, 20%, 30%, and 40%, with leeway (drift) angles ranging from  $\pm 5^\circ$  and rudder angles from  $-30^\circ$  to  $+30^\circ$  with  $10^\circ$  increments. The study provides physical insight into the relative interactions as well as a benchmark dataset for the effects of leeway and rudder angles on hydrodynamic forces and moments across different propeller loadings available for use in velocity prediction programs and for design. The results indicate that as the physical rudder angle increases, there is a corresponding increase in ship resistance, side force, and rudder-induced yaw moment that is dependent on propeller thrust loading and its flow straightening effect on the effective rudder angle. Analysis of drift-induced resistance provided valuable insights into efficiency tradeoffs in wind-powered ships implementation, including the net resistance penalty of hull leeway and rudder drag on required overall thrust. The relative contribution of rudder side force and yaw moment to the total side force and yaw moment is analyzed. For each tested leeway angle, the study identifies the required rudder angle to balance hydrodynamic-induced yaw moment, demonstrating the significant rudder adjustments necessary for wind-propelled ships and thereby the hull features that would be beneficial for future wind assist ship design.

© 2025 Author(s). All article content, except where otherwise noted, is licensed under a Creative Commons Attribution (CC BY) license (https:// creativecommons.org/licenses/by/4.0/). https://doi.org/10.1063/5.0281083

#### I. INTRODUCTION

In 2023, the International Maritime Organization (IMO) took a landmark step by revising its greenhouse gas (GHG) emissions reduction strategy, setting an ambitious goal of achieving net-zero emissions from ships "by or around 2050." These ambitious goals necessitate immediate actions from the shipbuilding industry. Among the various strategies proposed to reduce GHG emissions in the maritime industry, wind propulsion technologies have emerged as one of the most promising approaches. These innovative solutions, including soft sails,<sup>2,3</sup> kites,<sup>4</sup> Flettner rotors,<sup>5,6</sup> and wing sails,<sup>7,8</sup> offer significant potential for reducing fuel consumption and minimizing the environmental impact of commercial vessels.9-

The potential impact of wind-assisted ship propulsion (WASP) technologies is notable, as evidenced by many studies across various vessel types. 14-16 Recent investigations have demonstrated significant reductions in fuel consumption, with fuel savings ranging from 5.6% to 30% for Aframax oil tankers,<sup>5</sup> RoRo cargo ships,<sup>17</sup> and bulk carriers. 18 Moreover, a study on the integration of WASP systems into a slender bulk vessel demonstrates promising results, potentially reducing operational fuel consumption by up to 40% and GHG emissions by up to 30%. 19 Mason et al. 20 investigated the potential for reducing CO2 emissions in shipping by combining modern wind propulsion with voyage optimization. Their study on Panamax bulk carriers equipped with Flettner rotors revealed that this combination could achieve over 30% CO2 savings on favorable routes without altering arrival times, and up to 60% when including increased time flexibility. While one advantage of wind propulsion technologies is their ability to be retrofitted onto existing fleet vessels, they also present significant

<sup>&</sup>lt;sup>a)</sup>Author to whom correspondence should be addressed: S.Hosseinzadeh@soton.ac.uk

potential for incorporation into future ship designs during the concept phase. Plessas and Papanikolaou<sup>21</sup> developed a simulation tool to assess the performance of WASP, focusing on their effect during concept design. Applying this to a Very Large Crude Carrier (VLCC) tanker case study, they found that ships optimized for WASP differ from traditional designs. Later on, Arabnejad *et al.*<sup>22</sup> conducted a study on hybrid battery-hydrogen-WASP for a benchmark merchant ship in the Baltic Sea, demonstrating that the integration of four Flettner rotors as a WASP system achieved 35% reduction in required energy and 28% in power requirements.

Despite recent advancements in the development of WASP technologies, a knowledge gap persists regarding their optimal design, integration, and operational efficiency. A thorough analysis of a ship's thrust, drift, and yaw characteristics is essential for accurately assessing the fuel savings potential of wind propulsion systems. Additionally, precise performance predictions must account for two key factors: the increased resistance caused by rudder adjustments to counteract yaw moments generated by the sails, and the added resistance due to leeway from side forces. One of the main challenges lies in effectively capturing the complex interaction between aerodynamic forces and hydrodynamic behavior, particularly when vessels operate at leeway angles.<sup>23–26</sup> Kramer et al.<sup>27</sup> explored the effects of drift forces on ship resistance, comparing wing sails with Flettner rotors. Their study demonstrated that oversimplified models often lead to inaccurate estimates of drift-induced forces. Moreover, their findings showed that Flettner rotors produce higher side force-to-thrust ratios and contribute more to drift-related added resistance compared to wing sails. In further experimental work, Kramer et al.<sup>28</sup> examined the influence of leeway angle on drag, lift, and yaw moment using ship-like foil geometries with varying aspect ratios and bottom edge shapes. Comparing their experimental results with simplified models of lift and lift-induced drag, they concluded that slender body theory does not accurately predict these forces. Tillig and Ringsberg<sup>17</sup> used a ship performance model to evaluate generic cargo vessels and emphasized the need to account for the interaction effects between sails on wind-assisted ships.

Wind propulsion technologies, though effective in reducing required propeller thrust, introduce significant aerodynamic side forces that cause the ship to operate at leeway angles. This phenomenon not only affects the ship's course, <sup>29</sup> but also presents additional hydrodynamic complexities. The side forces create heel and yaw moments, requiring a delicate balance between hydrodynamic and aerodynamic forces to maintain a stable heading. <sup>30</sup> Achieving this balance demands sophisticated design approaches and possibly new control systems. Beyond simple force balancing, the altered flow regime around the hull can affect resistance characteristics, potentially impacting the speed-power relationship. <sup>31,32</sup> The propeller's performance is altered due to operating in the non-uniform wake caused by the leeway angle. <sup>33</sup> Similarly, the rudder's ability to maintain course stability may be diminished, requiring careful analysis and potential design modifications.

Although previous studies have primarily concentrated on predicting performance, optimizing routes, and evaluating the efficiency of different devices, a comprehensive investigation into the intricate interactions at the ship's stern, particularly the hull-propeller-rudder dynamics, is still necessary. Experimental studies on WASP provide valuable insights but also present unique challenges that must be addressed. One of the primary issues lies in the conflicting scaling requirements: traditional ship model tests rely on Froude scaling laws to accurately represent hydrodynamic behavior, whereas wind-assisted vessels require Reynolds number similarity and capturing the effective twist of the apparent wind with the atmospheric boundary layer. Achieving these scaling conditions simultaneously is practically impossible alongside the technical difficulty of creating a representative wind field in a towing tank. Bordogna et al.<sup>34</sup> tackled some of these issues by investigating the Reynolds number effect on the aerodynamic performance of wind-assisted vessels through a series of wind tunnel experiments using a Flettner rotor. However, their study did not consider hydrodynamic effects. To address these limitations, Sauder and Alterskjaer<sup>35</sup> introduced an innovative cyber-physical empirical method, originally developed for floating wind turbines, that integrates wind loads from previous numerical analyses into real-time ship motion simulations. While this method offers several advantages, the authors acknowledged that their simplified aerodynamic model did not fully capture key sail-hull and sail-sail interactions. Additionally, they noted that the semi-empirical equations used for calculating lift and drag coefficients for rotor sails introduced considerable uncertainty.

For wind assist, a proportion of the necessary thrust to achieve a required speed is provided by a conventional propeller. However, the same force/moment balance needs to be resolved to evaluate the operating condition of the propeller for a desired ship speed and heading. Physically, as with the sailing yacht, the wind-assisted device generates a side force, thrust, and yaw moment, which need to be balanced by the forces and moments due to the hull, propeller, rudder, and their interaction. The physics of this interaction is investigated in detail in this work using model-scale towing tank experiments with separately instrumented rudder, propeller, and hull. The relative importance of the hull leeway and the proportion of thrust delivered by the wind assist are the primary variables, which allow the magnitudes of the interaction effects to be determined.

This study focuses on key aspects of the hydrodynamic performance of wind-assisted ships, utilizing experimental methods on a self-propelled scaled model ship. The study has four primary objectives. First, it aims to establish a comprehensive experimental dataset of a self-propelled model with quantified uncertainties, serving as a benchmark for future numerical validations. Second, the research evaluates the influence of rudder and leeway angle on the vessel's total tow force, side force, and yaw moment across various propeller loading conditions. The third objective involves assessing rudder lift and drag forces under different leeway and rudder angle configurations. Finally, the study examines the ship's performance at its self-propulsion point, quantifying thrust reduction (attributed to wind assistance) as a percentage and analyzing its impact on side force, yaw moment, and the wind-powered vessel's performance. Such insights should help future ship designers when they consider what key attributes they need from the design of hull, propeller, and rudder.

#### II. EXPERIMENTAL METHOD

This series of experiments was conducted in the University of Southampton's Boldrewood towing tank, which is 138 m long, 6 m wide, and 3.5 m deep.<sup>36</sup> The details of the towing tank, including carriage specifications, wave makers, and other facilities, are provided in Refs. 29, 30, and 37.

#### A. Scaled ship geometry

A scaled geosim model of the KRISO Container Ship (KCS) hull form,  $^{38}$  was constructed using laser-cut plywood frames and strip planks and finished with a hydrodynamically smooth paint (see Table I), with a scale ratio of  $\lambda=1/60.96$  (hereinafter referred to as the UoS model). Standard trip studs were placed at 5% of the length from the bow. Figure 1 illustrates the details of test setup, and instruments used in this series of experiments. The model was equipped with a propulsion system comprising a motor and propeller. The power was supplied by two sets of lithium-ion batteries, ensuring up to 8 h of continuous operation. A reaction torque load cell, installed on the electric motor casing, enabled measurement of propeller torque. The motor was mounted on a slide, which allowed for the measurement of propeller thrust, with an optical sensor for RPM (revolutions per minute) measurement. The propeller RPM was set using a proportional controller integrated with a modified radio controller unit.

The model was equipped with an all-movable rudder (NACA 0018 profile) with the same planform as the original semi-balanced skeg rudder [Figs. 1(b) and 1(d)]. The rudder was controlled by a radio control unit that could either fix a calibrated rudder angle or vary it as needed. Additionally, a high-quality, titanium alloy KP505 propeller was fabricated and utilized in the self-propelled tests [Fig. 1(c)]. The specifications of the rudder and propeller are detailed in Table I.

#### B. Test setup

Figure 1(a) depicts the test setup installed on the carriage. The model was attached to the towing tank carriage at two points (twinpost system) to measure side forces. As shown in Fig. 1(a), the main post and second post are positioned at 2.5 and 1.5 m from the stern,

**TABLE I.** Main particulars of KCS hall [Reproduced with permission from Hosseinzadeh *et al.*, Data Brief **58**, 111257 (2025). Copyright 2025 Authors, licensed under a Creative Commons Attribution (CC BY-NC-ND) license].<sup>37</sup>

Parameters	Unit	Full-scale	UoS model	
Scale (λ)		1	60.96	
Displacement (tonne)	tonne	52 030	0.23	
Depth (m)	M	19.0	0.312	
Breadth (B)	M	32.2	0.528	
$L_{PP}$	M	230	3.773	
$L_{WL}$	M	232.5	3.814	
Draft amidships (d)	M	10.8	0.177	
KCS rudder		NACA 0018		
Wetted area rudder (A <sub>R</sub> )	$m^2$	115	0.031	
Wetted surface area	$m^2$	9539	2.567	
(hull+rudder) (A <sub>m</sub> )				
Propeller		KP505 (NACA 66)		
		5 blade		
Propeller diameter (D <sub>P</sub> )	m	7.9	0.13	
$A_e/A_o$		0.8	0.8	
Propeller rotation		Clockwise	Clockwise	
direction (from stern)				
Average water		• • •	16.3 °C	
temperature				

respectively. The yaw pivot point, which creates the leeway angle, is 2.0 m from the stern, centered between the main and second posts. In addition, the rudder dynamometer is positioned 98.43 mm from the stern and 261.08 mm from the keel of the model. To conduct experiments at different leeway angles, a twin plate adjustment system was used. A schematic view of the leeway angle adjustment mechanism for 0° and 5° is shown in Fig. 2. The motion of the model is constrained to heave and pitch about the tank centerline rather than the ship axis system. The main data were gathered in the tank axis system, while the rudder dynamometer data were recorded in the ship axis system. The coordinate system used during the experiment is depicted in Fig. 3, adhering to the right-hand rule for both the model and the rudder.

# C. DAQ system and test plan

All sensors were calibrated to ensure the reliability of data and minimize experimental uncertainty. The details of the calibration procedure are explained in Hosseinzadeh  $et\ al.^{37}$  An onboard data acquisition (DAQ) system was used to collect data from 16 channels. For each run, the DAQ recorded model drag, two side force channels, heave, trim, carriage speed, propeller thrust, torque, and rpm, six rudder force and moment components, and wave height. The twin-post system allows measurement of yaw moment. The side forces were measured using an additional force block mounted at the base of the twin post. The details of the laser-based system used to measure the carriage position and speed can be found in Malas  $et\ al.^{36}$ 

A six components rudder dynamometer was utilized to measure rudder forces and moments. The six strain gauge outputs were processed using a manufacturer supplied interaction matrix to determine the forces  $(F_{xR}, F_{vR}, F_{zR})$  in Newtons, as well as the moments  $(T_{xR}, T_{vR}, T_{vR})$ TzR) in Newton-meters. Following each run, the recorded data were assessed for consistency before proceeding to the next run. A sampling rate of 200 Hz was maintained for all collected data, ensuring highresolution and accurate measurements throughout the experiment. The mass of the bare hull and all instrumentation was measured separately to precisely align with the designed loading condition. The experimental details are summarized in Table II. The propeller advance ratio, J, is defined as  $J = V_m/nD$ , where  $V_m$  is the towing speed, n is the propeller's rotational speed, and D is the propeller diameter. As shown in Table II, self-propelled experiments were conducted at various propeller RPMs for each leeway and rudder angle, ranging from RPM<sub>1</sub> to RPM<sub>4</sub>. The tested conditions correspond to  $RPM_1 = 458 \text{ rpm}$   $(J_1 = 1.195)$ ,  $RPM_2 = 554 \text{ rpm}$   $(J_2 = 0.988)$ ,  $RPM_3 = 644 \text{ rpm } (J_3 = 0.850), \text{ and } RPM_4 = 768 \text{ rpm } (J_4 = 0.713).$  The offloaded propeller conditions were applied as controlled reductions in propeller thrust, simulating the effect of an external wind force contributing to the vessel's propulsion. This approach allows us to systematically investigate the hydrodynamic response of the hull, rudder, and propeller without introducing the aerodynamic scaling challenges of applying real wind forces in the towing tank. The experiments primarily focused on varying rudder and leeway angles while testing different propeller loadings to simulate varying proportions of thrust contribution from the wind.

## **III. DATA PROCESSING**

The data collection process encompassed the entire length of each run, with each run including multiple conditions: four carriage speeds for conventional resistance tests and four different rudder

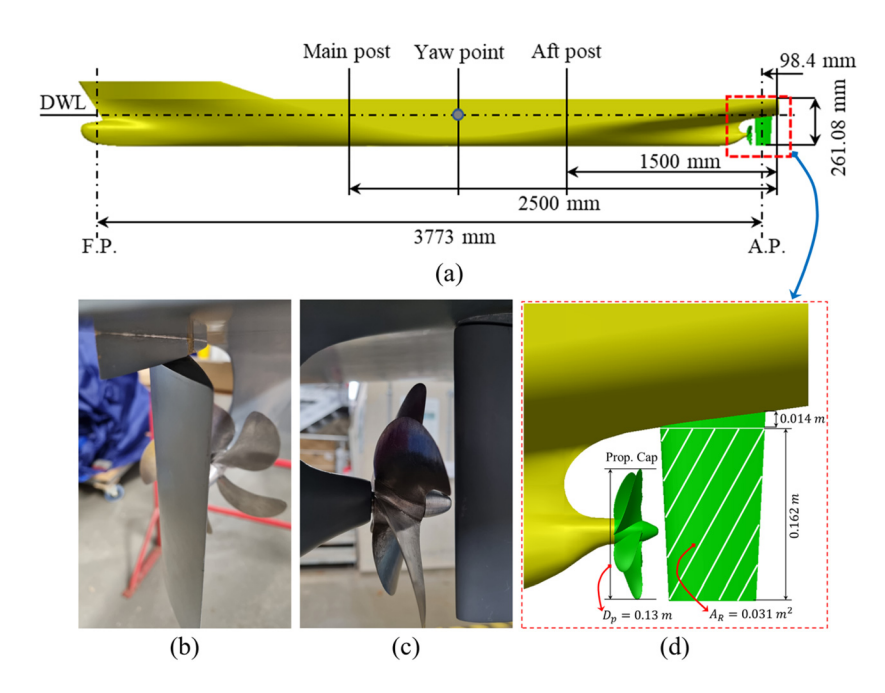


FIG. 1. Experiments setup and the model geometry (a) schematic view of the twinpost setup [Modified with permission from Turnock et al., Ocean Eng. 312(3), 119258 (2024). Copyright 2024 Authors, licensed under a Creative Commons Attribution (CC BY) license], (b) KCS rudder installed to the model; (c) KP505 propeller model; (d) details of the propeller and rudder properties.

angles for the other tests. As a result, an initial trimming process was necessary to separate these different conditions. This process involved segmenting the data into specific test segments by identifying the start and finish points of each run. The trimmed sections were determined by observing changes in rudder force, carriage speed, and in some cases, propeller RPM. For detailed information on the trimming process, refer to Hosseinzadeh *et al.*<sup>37</sup>

### A. Uncertainty analysis

To enhance the quality of the measured data and filter out the high-frequency noise from the recorded signal, a low-pass filter is applied to the raw data. The filters are generated by employing a "filt-filt" function, <sup>39</sup> which is a zero-phase digital filtering technique that processes the current point in relation to both forward and reverse

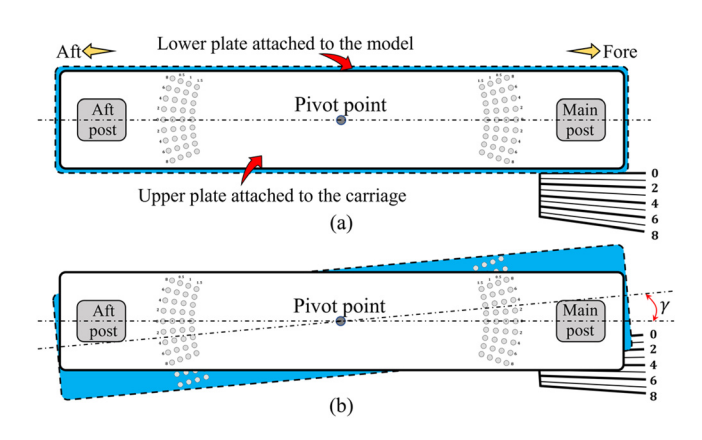


FIG. 2. Schematic view of the leeway angle adjustment mechanism: (a) zero leeway angle; (b)  $+5^{\circ}$  leeway angle.

points in the frequency domain to retain the signal time history in line with the original signal. Comparison of the mean values between the original and filtered signals confirms that the error between the filtered signal with a 10 Hz cutoff frequency and the mean value of the original signal is 0.32% for drag and 0.028% for rudder force. Therefore, it can be concluded that the selected cutoff frequency has a

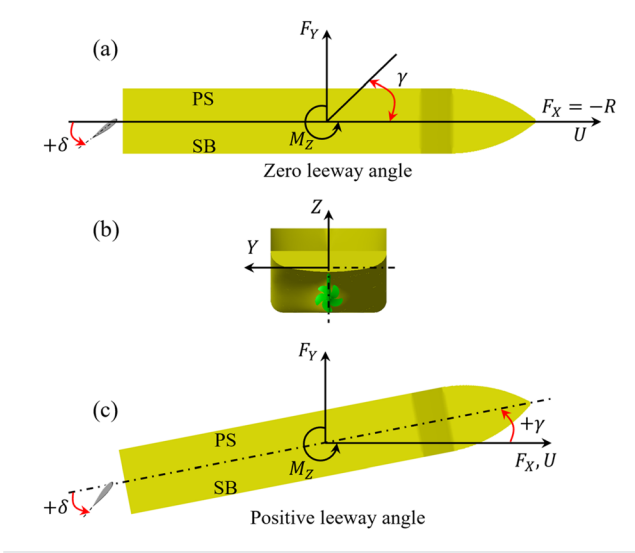


FIG. 3. Coordinate systems used for data measurement during the experiments: (a) schematic top view showing that primary data were measured in the tank-axis system, while rudder dynamometer data were recorded in the ship-axis system (with side force defined as positive to port); (b) stern view of the model; (c) the model under a positive leeway angle.

TABLE II. Test matrix of the appended hull, no propeller, and self-propelled model experiments (water temperature = 16.3 °C).

Conventional re	esistance test						
V <sub>s</sub> (knots)	V <sub>m</sub> (m/s)	F <sub>n</sub> (-)	Leeway angle (°)	Rudder angle (°)	Propeller RPM		
10.00	0.659	0.11					
14.00	0.922	0.15					
18.00	1.186	0.19	_				
21.00	1.384	0.23	0	0	w/o propeller, with rudder		
24.00	1.581	0.26					
26.00	1.713	0.28					
Non-propelled	tests						
			-5	$0, \pm 10, \pm 20, \pm 30$			
			-2.5	$0, \pm 10, \pm 20, \pm 30$			
			-1	$0, \pm 10, \pm 20, \pm 30$			
18.00	1.186	0.195	0	$0, \pm 10, \pm 20, \pm 30$	w/o propeller, with rudder		
10.00			1	$0, \pm 10, \pm 20, \pm 30$	1 1 1		
			2.5	$0, \pm 10, \pm 20, \pm 30$			
			5	$0, \pm 10, \pm 20, \pm 30$			
Self-propelled	experiments						
			-5	$0, \pm 10, \pm 20, \pm 30$	$RPM_1$ to $RPM_4$		
			-2.5	$0, \pm 10, \pm 20, \pm 30$	$RPM_1$ to $RPM_4$		
			-1	$0, \pm 10, \pm 20, \pm 30$	$RPM_1$ to $RPM_4$		
18.00	1.186	0.195	0	$0, \pm 10, \pm 20, \pm 30$	RPM <sub>1</sub> to RPM <sub>4</sub>		
			1	$0, \pm 10, \pm 20, \pm 30$	$RPM_1$ to $RPM_4$		
			2.5	$0, \pm 10, \pm 20, \pm 30$	RPM <sub>1</sub> to RPM <sub>4</sub>		
			5	$0, \pm 10, \pm 20, \pm 30$	$RPM_1$ to $RPM_4$		

negligible to no effect on the results and is thus applied to all sensors for the rest of the runs.

Table III provides an analysis of repeatability across three test conditions, all conducted at zero leeway and zero rudder angle. It presents the average of signals' means and standard deviations for all 16 channels at three different RPM settings. The number of repeat (N) runs varies from 4 to 5 across these conditions. The data reveals important trends, with standard deviations providing insight into measurement variability. Most parameters exhibit relatively low standard deviations, indicating good repeatability. However, increasing the propeller speed amplifies the discrepancy in standard deviations. This is particularly evident in the shaft RPM measurements, where the 768 RPM setting shows a notably higher standard deviation (16.38) compared to lower RPM settings, suggesting increased variability at higher rotational speeds. This observation points to a potential correlation between increased propeller speed and reduced measurement consistency. The consistency observed across repeated runs and different conditions provides confidence in the reliability of the collected data for further analysis.

#### B. Calm water resistance (hull with rudder appendage)

Experiments conducted on the KCS hull offer valuable opportunities for comparison with decades of test data on this model, particularly from the CFD validation workshop. To further assess the accuracy of our experiments, we compared data from six separate tests (utilizing the same setup but conducted on different dates) with the TOKYO'15

data. These tests were carried out at various model speeds with zero leeway angle, zero rudder angle, and no propeller, representing calm water conditions for the bare hull with rudder appendage. Table IV provides detailed information on the experimental measurements collected from September 2022 to February 2024. To facilitate comparison with historical test data from the UoS model and TOKYO'15 data, the recorded total resistance data were rescaled to  $15\,^{\circ}$ C ( $R_{\rm TMIS}$ ).

Table IV provides key metrics, including the standard deviation  $(\sigma)$ , relative standard deviation (RSD), standard uncertainty  $(u_A)$ , expanded uncertainty (UA), and combined uncertainty (UC), following the ITTC uncertainty analysis guidelines for resistance tests.<sup>40</sup> The RSD percentages are generally low, ranging from 1.07% to 2.73%, indicating good repeatability across the tests. The standard uncertainty reflects the precision of the measurements, calculated as  $(\sigma/\sqrt{N}) \times 100$ , where n is the number of measurements. The expanded uncertainty (U<sub>A</sub> = ku<sub>A</sub>) represents the uncertainty at the 95% confidence level by the Type A method, using a coverage factor of k = 2. Furthermore, the table includes the combined uncertainty (U<sub>C</sub>), which incorporates additional sources of uncertainty, including factors such as dynamometer accuracy. The data shows that the relative standard deviation is lower at mid-range speeds and higher at both lower and upper speed ranges. This variation suggests greater consistency in resistance measurements at mid-range speeds, with more noticeable discrepancies at high speeds. The comparison of the total resistance data is further illustrated in Fig. 4, offering a visual representation of how the resistance changes with different model speeds and showing the trends observed

TABLE III. Repeatability analysis of recorded variables at three different test conditions (zero leeway and zero rudder angles).

	$\frac{\text{RPM}_2 = 554}{\text{Number of repeats (N = 5)}}$		RPM <sub>3</sub> =	$\frac{\text{RPM}_3 = 644}{\text{Number of repeats (N = 4)}}$		$\frac{\text{RPM}_4 = 768}{\text{Number of repeats (N = 4)}}$	
			Number of rep				
Parameters	Mean (x̄)	σ	Mean (x̄)	σ	Mean (x̄)	σ	
Thrust (N)	4.440	0.335	7.121	0.118	11.563	0.796	
Torque (Nm)	-0.096	0.001	-0.153	0.001	-0.238	0.014	
Shaft (rpm)	554.0	0.348	644.0	0.950	768.0	16.380	
Carriage speed (m/s)	1.186	0.0003	1.185	0.0004	1.186	0.001	
Drag (N)	4.016	0.101	1.507	0.086	-2.444	0.610	
Side force (N)	0.109	0.107	0.330	0.171	0.415	0.161	
Yaw moment (Nm)	-0.833	0.449	-0.764	0.239	-0.799	0.212	
Trim (°)	0.091	0.015	0.086	0.004	0.081	0.007	
Heave (mm)	-4.539	0.178	-4.605	0.199	-4.595	0.282	
Shaft power (watts)	5.599	0.063	10.307	0.038	18.798	1.539	
F <sub>xR</sub> -rudder (N)	0.293	0.007	0.343	0.003	0.418	0.010	
F <sub>vR</sub> -rudder (N)	0.185	0.033	0.261	0.041	0.328	0.054	
F <sub>zR</sub> -rudder (N)	0.071	0.025	0.048	0.010	0.007	0.010	
T <sub>xR</sub> -rudder (Nm)	-0.078	0.006	-0.107	0.007	-0.139	0.008	
T <sub>vR</sub> -rudder (Nm)	0.054	0.0005	0.063	0.0003	0.075	0.001	
T <sub>zR</sub> -rudder (Nm)	0.010	0.0005	0.013	0.001	0.017	0.002	

in Table IV. The remaining tests were conducted at a constant model speed of 1.186 m/s.

#### C. Flow visualization around the hull

To elucidate the influence of leeway angle on flow development around the hull, surface flow patterns around the model are analyzed using optical flow visualization techniques. The Farneback algorithm<sup>57</sup> is applied to consecutive video frames captured during model tests to quantify surface velocity disturbances. This approach enables non-intrusive measurement of water surface motion, providing detailed insight into the complex flow field development around the hull under varying leeway conditions. The analysis processed all available frames within the measurement window to ensure temporal stability and statistical reliability of the flow field characterization.

TABLE IV. Measured total resistance data (rescaled to 15 °C) at different model speeds, standard deviation, expanded uncertainty (k = 2), and combined uncertainty.

Total resistance ( $R_{TM15}$ ) rescaled to 15 $^{\circ}C$						
$\overline{F_n}$	0.11	0.15	0.19	0.23	0.26	0.28
$V_{\rm m}$ (m/s)	0.659	0.922	1.186	1.384	1.581	1.713
Sep-22	2.512	4.809	7.437	10.113	13.771	18.946
Nov-22	2.555	4.864	7.567	10.351	14.319	20.003
June-23	2.560	4.859	7.425	9.899	13.720	18.511
July-23	2.470	4.790	7.470	10.080	13.880	18.680
Nov-23	2.476	4.660	7.363	10.018	13.902	18.968
Feb-24	2.417	4.710	7.558	10.276	13.957	19.054
Mean (x̄)	2.498	4.782	7.470	10.123	13.925	19.027
$\sigma$	0.055	0.082	0.080	0.167	0.212	0.519
RSD (%)	2.201	1.711	1.068	1.645	1.522	2.730
u <sub>A</sub> (%)	0.898	0.699	0.436	0.672	0.621	1.115
U <sub>A</sub> (%)	4.401	3.422	2.135	3.290	3.044	5.460
U <sub>C</sub> (%)	2.033	1.690	1.289	1.645	1.564	2.423
$R_{TM15}(N)$	$2.50 \pm 0.051$	$4.78 \pm 0.081$	$7.47 \pm 0.096$	$10.12 \pm 0.167$	$13.92 \pm 0.218$	$19.03 \pm 0.461$
R <sub>T</sub> (N) TOKYO'15	2.492	4.647	7.308	9.875	13.611	18.904

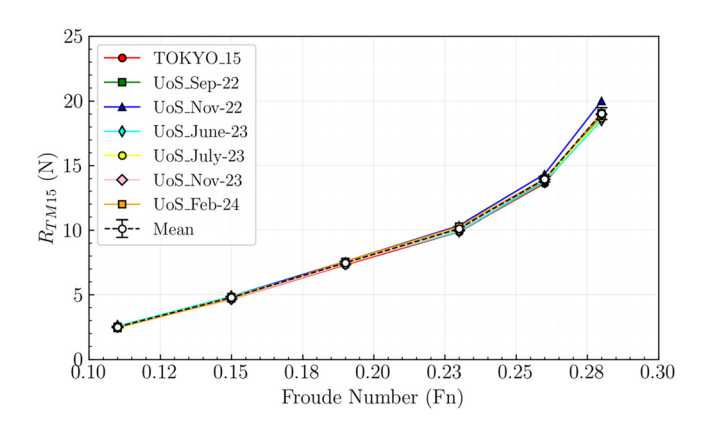


FIG. 4. Appended hull calm water total resistance at with combined standard uncertainty at 15  $^{\circ}\text{C}.$ 

Video sequences are processed using a multi-stage smoothing approach combining median filtering, Gaussian smoothing, and morphological operations to enhance signal quality while preserving flow features. Surface disturbance magnitude is calculated as the normalized optical flow velocity magnitude, representing the relative intensity of surface motion. A consistent colormap scale (0–8) is applied across all test conditions to enable direct comparison of disturbance levels

between different leeway angles. The water surface region is manually segmented to isolate hull-induced flow effects from background disturbances.

The flow visualization reveals a clear progression in surface disturbance intensity with increasing leeway angle magnitude. At  $\beta=2.5^\circ,$  minimal disturbance is observed with localized effects primarily concentrated near the stern due to propeller operation. The  $\gamma=5^\circ$  condition shows increased flow complexity around the hull with modified wave patterns, indicating enhanced hull-flow interaction and asymmetric flow development. The  $\gamma=-5^\circ$  case exhibits the most significant flow disturbances in both forward and aft regions, demonstrating substantial alteration of the flow field topology. This asymmetric flow behavior directly correlates with the measured side force and yaw moment trends, providing visual validation of the underlying flow physics responsible for the hydrodynamic force generation.

The observed flow patterns reflect the fundamental changes in boundary layer separation, pressure distribution, and wake development as the hull operates at an angle to the flow. The progressive increase in surface disturbance intensity with leeway angle magnitude indicates enhanced vorticity generation and turbulent mixing in the near-field region. These flow field modifications have direct implications for downstream wake characteristics and energy losses, supporting the measured trends in hydrodynamic resistance and lateral forces (see Sec. IV) (Fig. 5).

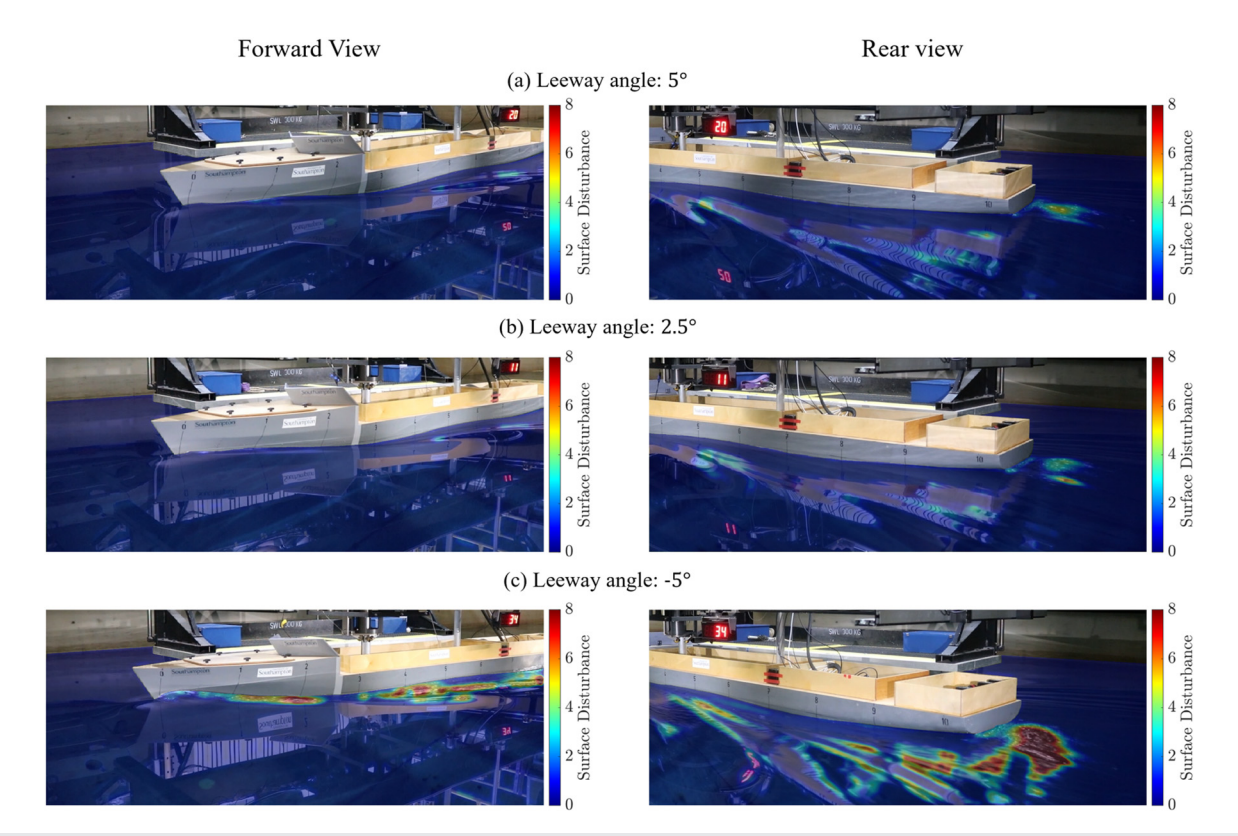


**FIG. 5.** Surface disturbance patterns around the hull at different leeway angles: (a)  $\gamma=5^\circ$ ; (b)  $\gamma=2.5^\circ$ , and (c)  $\gamma=-5^\circ$  for forward and rear views, respectively. The colormap represents normalized optical flow magnitude, indicating relative surface velocity disturbances. Propeller operating at RPM<sub>2</sub>. Clear progression in flow complexity and wake patterns demonstrates the significant influence of leeway angle on hull-flow interaction and downstream flow development.

#### IV. ANALYSIS OF FORCES AND MOMENTS

The findings are structured into three key subsections, each offering insights into the behavior of a wind-assisted ship (WAS) under different conditions. First, the measured forces and moments acting on the model are presented. Next, the rudder forces and moments, crucial elements in understanding wind-propelled vessels, are provided. Finally, the implications for the practical application of wind-assisted propulsion at the ship's self-propulsion point are discussed.

#### A. Model forces and moments

Figure 6 presents the measured total tow force coefficient ( $C_T$ ) as a function of rudder angle for various propeller speeds and leeway angles ( $\gamma$ ). The total tow force coefficient is defined as  $C_X = F_X/(0.5\rho A_w V_m^2)$ , where  $F_X$  is the measured towing force,  $\rho$  is water density,  $A_w$  is the model's wetted surface area (including hull and rudder), and  $V_m$  is the model speed. Propeller speeds were preset using a remote controller, with target RPMs for each run detailed in Table II. However, the actual measured shaft RPM varied slightly under different conditions, particularly at high rudder and leeway angles (see Fig. 12).

The total tow force consistently increases with increasing rudder angle, regardless of direction, across all propeller speeds and leeway angles. This can be attributed to the enhanced form and induced drag associated with larger rudder angles. Conversely, higher propeller speeds and increased thrust generally lead to reduced tow force coefficients, with the propeller-generated thrust partially offsetting the model's total tow force. Furthermore, it is found that the total tow force rises with increasing leeway angles, with this effect being more noticeable at negative leeway angles for propelled conditions, especially when the rudder angle is large. This asymmetry may stem from the complex flow dynamics around the model's transom, where the interaction between the drift-induced flow, direction of rotation of the propeller, and rudder becomes significant. 41 The tow force curves show a slight imbalance around the zero-rudder angle, particularly in cases of nonzero leeway angles. This asymmetry is likely a result of the single-screw propeller configuration, which produces an uneven flow field around the propeller, thereby influencing rudder performance. 42,4

Tests were conducted without the propeller to investigate the drift-induced resistance. The comparison between the total tow force of zero and non-zero leeway angles for the non-propelled cases showed a 22% increase in the total tow force coefficient at a +5° leeway angle. The results of non-propelled cases, depicted in the "w/o prop." curves in Fig. 6, show how the rudder alters the effective camber of the hull, like an aircraft wing flap, inducing hull side force and resultant increase in drag.

Figure 7 illustrates the influence of leeway and rudder angles on the side force coefficient at different propeller speeds, plotting the total side force coefficient  $[C_S = F_Y/(0.5\rho A_w V_m^2)]$  as a function of rudder angle for various propeller speeds and leeway angles. As the magnitude of the rudder angle increases, the side force coefficient generally rises. This is expected since the rudder produces lift (side force) in proportion to its angle of attack. For small to moderate rudder angles, the relationship between rudder angle and side force appears nearly linear. However, this linearity breaks down at higher rudder angles, particularly beyond  $\pm 20^\circ$ , where the side force no longer increases at the same rate and may even decline if the rudder stalls or due to the effect of leeway angle on the hull–rudder interaction.  $^{41,43}$  Further

investigation into side force is conducted in non-propelled conditions (w/o prop.), allowing a comparison of side force coefficients between these and self-propelled scenarios. The curve reveals the additional side force generated by the rudder under self-propelled conditions, indicating the importance of including the accelerated flow over the rudder when predicting hydrodynamic side force, and providing insight into the rudder's effect on overall side force production.

The effect of propeller speed on the side force coefficient is also clearly noticeable. As propeller speed increases, the side force coefficient tends to increase for a given rudder angle. This is due to the higher flow velocity over the rudder surface, caused by the propeller, enhancing its effectiveness. The leeway angle plays a crucial role in shaping the side force behavior. At a leeway angle of  $\gamma=0^\circ$ , the curves are almost symmetrical about the zero-rudder angle. However, when the leeway angle is non-zero, the curves shift noticeably. This shift confirms that the hull itself generates side force when subjected to a leeway angle, which then combines with the rudder-generated force to form the total side force acting on the vessel.

Figure 8 presents the yaw moment coefficient [C<sub>N</sub>  $=M_{Z}/(0.5 \rho A_{w} \; L_{pp} V_{m}^{\;\;2})]$  plotted against the rudder angle for various leeway angles. The relationship between rudder angle and yaw moment coefficient is consistent across all leeway angles. At zero rudder and leeway angle, the yaw moment coefficient is approximately zero, as expected. As the rudder angle becomes more positive or negative, the yaw moment coefficient shows a near-linear increase or decrease, respectively. This indicates that the rudder has a direct and proportional effect on the yaw moment, with larger rudder angles leading to larger yaw moments. The influence of the leeway angle on the yaw moment is also significant. At  $\gamma = 0^{\circ}$ , the curves are symmetrical about the zero-rudder angle, with positive and negative yaw moments being almost mirror images. However, as the leeway angle increases, the yaw moment generated by the hull becomes more significant and the curves become asymmetric, especially at higher rudder angles. This asymmetry indicates that the hull's leeway angle alters the rudder's effect depending on whether the leeway is to port or starboard. The comparison between the self-propelled and non-propelled cases also highlights the substantial role the propeller plays in enhancing the yaw moment. It is likely that a wind-assisted ship will, as a result, perform better, e.g., can sail at a smaller leeway angle for either an apparent wind angle from port or starboard, depending on its propeller direction of rotation.33

#### B. Rudder data

A rudder dynamometer was used to measure the forces and moments acting on the rudder in the ship's axis system, allowing its side force and drag to be examined in detail. Figures 9 and 10 illustrate the rudder drag  $[C_{DR}=F_{xR}/(0.5\rho A_R V_m^2)]$  and lift  $[C_{SR}=F_{yR}/(0.5\rho A_R V_m^2)]$  coefficients, respectively, plotted against rudder angle for various leeway angles.  $A_R$  is based on the rudder's surface area rather than the total wetted surface area, as this subsection focuses solely on rudder data. For a direct comparison between the total side force and the rudder side force, the same wetted surface area ( $A_{w}$ ) is used for both  $C_S$  and  $C_{SR}$ . Moreover, as mentioned earlier, the rudder dynamometer data were collected in the ship's axis rather than the tank's axis. The drag coefficient exhibits a symmetrical pattern around the zero-rudder angle at lower rudder angles and propeller speeds. However, this behavior changes under more extreme conditions,

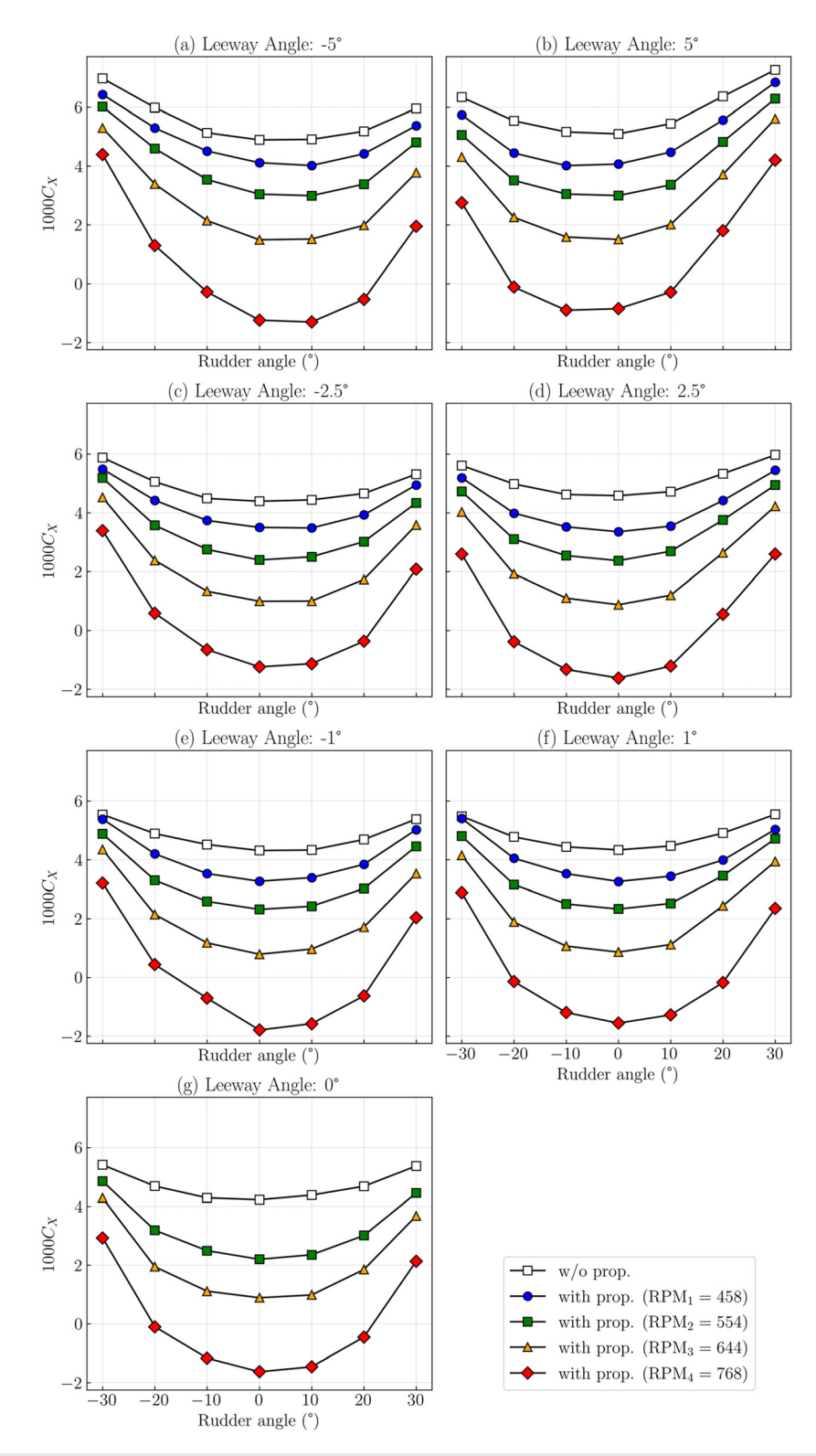


FIG. 6. Influence of rudder angle and propeller speed on the model's total tow force coefficient at different leeway angles and propeller RPMs; including the comparison with non-propelled hull (w/o prop.).

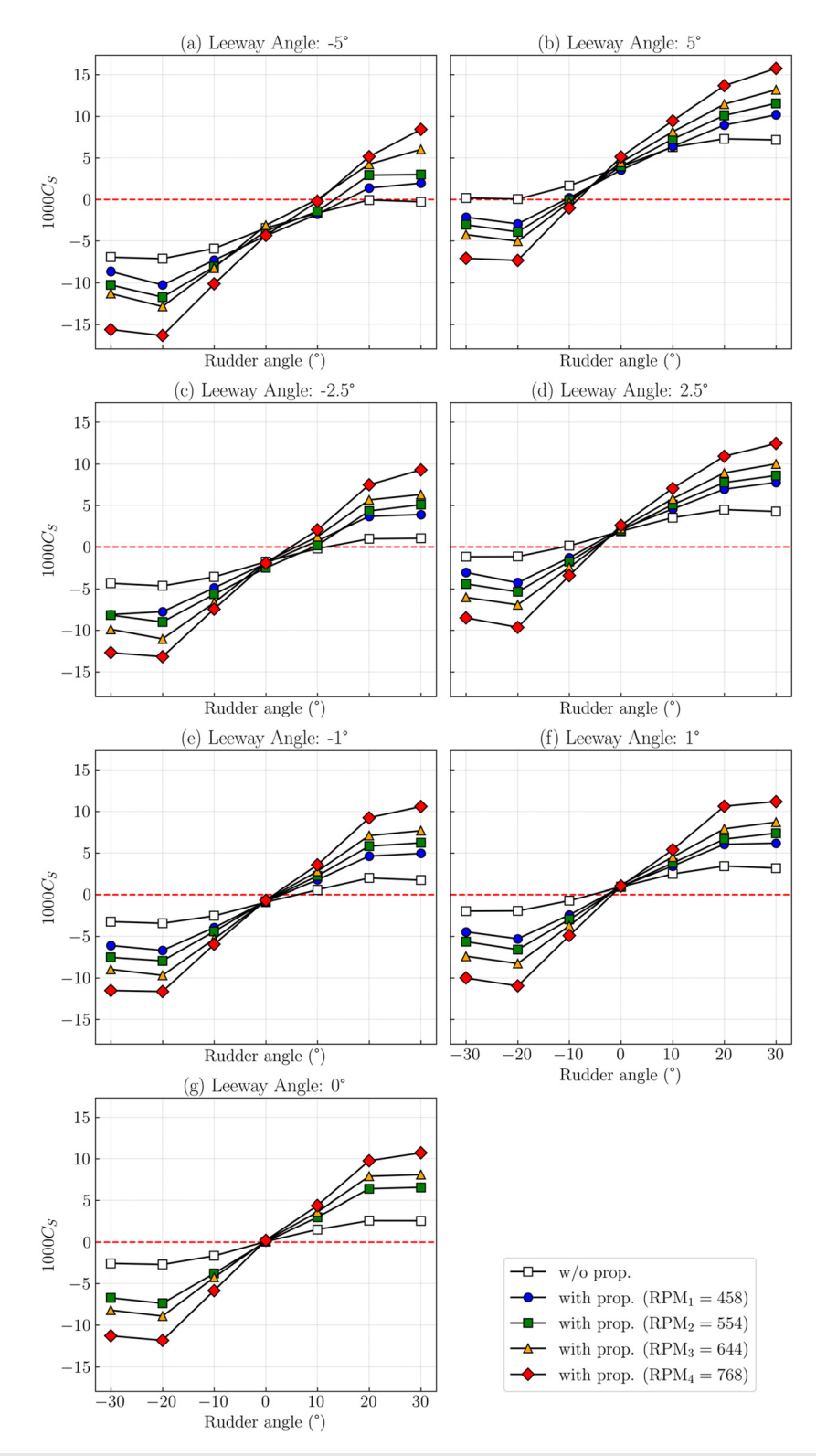


FIG. 7. Influence of rudder angle and propeller speed on the model's total side force coefficient at different leeway angles and propeller RPMs; including the comparison with non-propelled hull (w/o prop.).

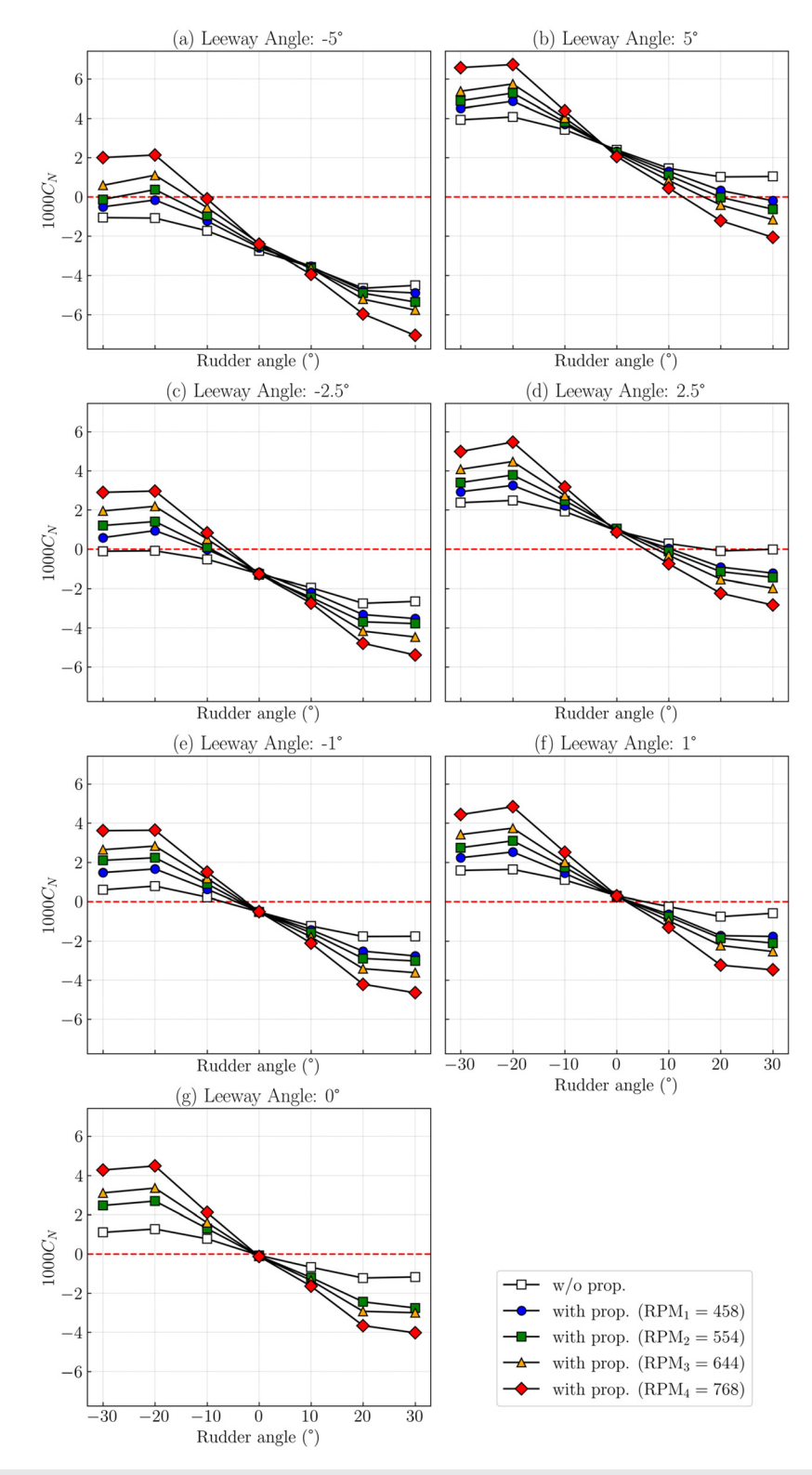


FIG. 8. Effect of rudder angle and propeller speed on the model's yaw moment coefficient at different leeway angles and propeller RPMs; including the comparison with non-propelled hull (w/o prop.).

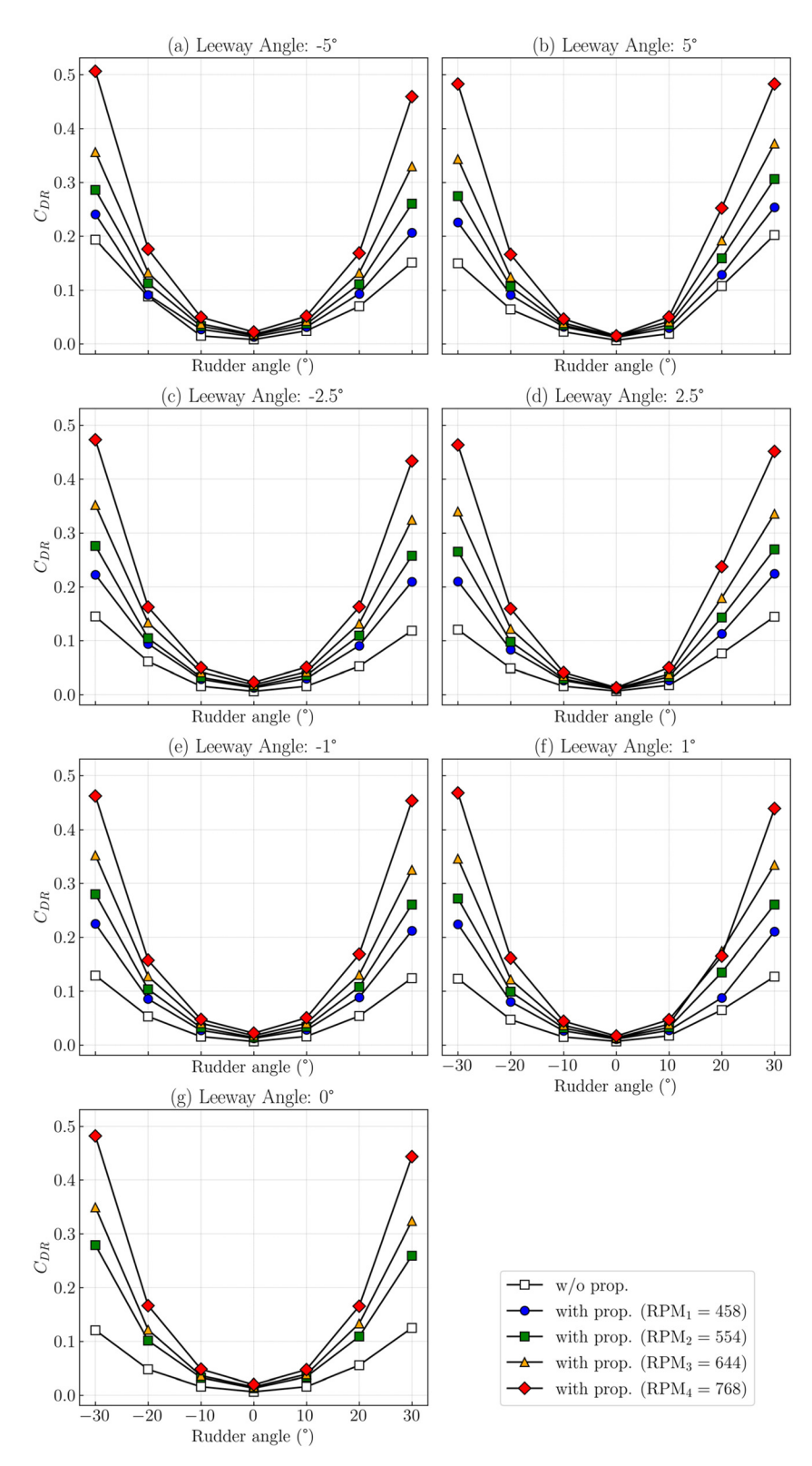


FIG. 9. Influence of rudder and leeway angles on the rudder drag coefficient (C<sub>DR</sub>) at various propeller speeds and in non-propelled conditions.

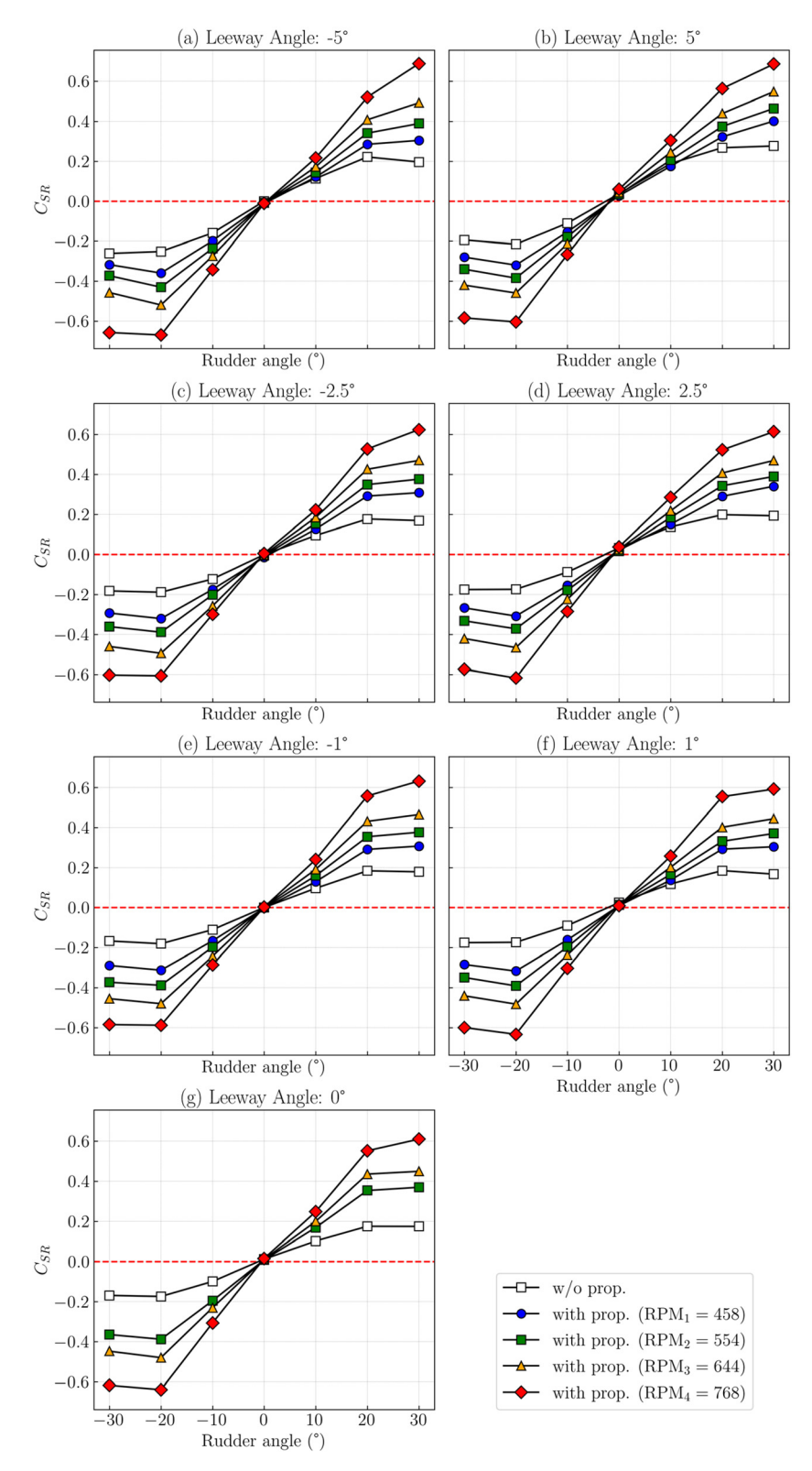


FIG. 10. Influence of rudder and leeway angles on the rudder lift coefficient (C<sub>SR</sub>) at various propeller speeds and in non-propelled conditions.

particularly at higher rudder angles. This is expected due to the side force of rudder. Interestingly, the non-propelled case consistently exhibits lower drag across the entire rudder range compared to the self-propelled cases. The propeller's race increases the flow velocity over the rudder, resultant side force, and associated induced drag. As the propeller RPM increases, so does the propeller thrust loading, with the highest RPM case showing the greatest drag increase. At smaller rudder angles, the differences in drag between the propelled and non-propelled cases are relatively minor; however, at higher rudder angles, the gap widens, confirming the role of the propeller in increasing drag at greater rudder angles. This effect is unlikely to be of benefit for wind assist ships as they will typically have a leeway angle and a larger rudder angle to achieve a net zero yaw moment.

The rudder side force coefficient follows a linear trend for the rudder angle below  $\pm 20^\circ$ , increasing as the rudder angle magnitude grows. This is because the rudder generates lift based on its angle of attack. The non-propelled case generates the lowest lift values. As with drag, the differences between self-propelled and non-propelled cases become more noticeable at higher rudder angles. In addition, the results highlight that the impact of leeway angle on rudder forces is minimal under propelled conditions, likely due to flow straightening caused by the propeller.  $^{41}$ 

#### V. APPLICATION TO WIND PROPULSION

As explained, wind-assisted devices offer the potential for significant energy savings. There are a variety of possible devices that effectively capture energy from the wind and generate a thrust offset, so less power is required from a propeller. Their operation is based on the well-understood physical principles of a sailing craft, where the developed aerodynamic forces and moments of the sail system and superstructure are balanced by the underwater hydrodynamic forces and moments of the hull and appendages. <sup>29,30,45,46</sup> In steady conditions, the balance of these aero/hydrodynamic forces will give a steady speed to the vessel with an effective leeway and heel angle. Trimming the sails and adjusting the rudder angle can ensure the ship achieves the fastest Velocity Made Good (VMG) for a given heading and wind direction. The balancing process allows the two domains to be treated in isolation.

For wind-assisted ships (WAS), the self-propulsion point (SPP) will be dependent on the true wind speed, direction, and ship speed through the water. As with a sailing yacht, the wind assist device will be adjusted to maximize the velocity made good. For a WAS, VMG can be interpreted as the least propulsive power for VMG. In analyzing sailing yacht performance, a velocity prediction program (VPP) is used to find the operating point for given wind conditions. <sup>45,47,48</sup> This uses, in its more advanced form, a six degree of freedom force/moment balancing process. The data measured provides the tow force, side force, and moment capabilities for such a VPP process. In the following analysis, we have assumed a proportion of the required thrust for that given condition (leeway angle, rudder angle, and propeller RPM) will be provided by the WAS.

#### A. Derived data

A comprehensive understanding of the hydrodynamic performance of wind-assisted vessels requires analyzing results at the ship's self-propulsion point. This method offers a realistic and precise evaluation of performance, which is essential for both design and operational

decision-making. The full-scale self-propulsion point was identified using the load-varying method at a constant speed, in accordance with ITTC propulsion test procedures. The skin friction correction force, denoted as  $F_D$  ( $F_D\!=\!0.5\rho A_m V_m^2$  [(1+k)( $C_{FM}-C_{FS})-\Delta C_F$ ]), was calculated based on these procedures. In this equation,  $C_{FM}$  represents the frictional resistance coefficient of the model,  $C_{FS}$  is the frictional resistance coefficient of the ship,  $\Delta C_F$  accounts for roughness allowance, and (1+k) is the form factor. It is worth noting that  $F_D$  is assumed to remain constant despite changes in leeway and rudder angles. This correction force adjusts for the difference in frictional resistance between the model and the full-scale ship due to the Reynolds number effect.

To make the findings more applicable to WAS, we present the subsequent data in terms of the percentage of thrust provided by the wind (0–40%). For example, a "10% reduction thrust" indicates that we assume wind contributes 10% of the total required thrust. Figure 11 shows the method that is applied to calculate the reduction thrust based on the thrust value at the ship's self-propulsion point. The solid green lines indicate the thrust and tow force at the SSP, where  $\delta=0$  and  $\gamma=0$ . To simulate a thrust reduction (e.g., 20%), the corresponding new skin friction correction force  $F_D^{new}$  is calculated by adding a proportion of the thrust at SSP to the original force  $(F_D^{new}=F_D+0.2\times T_{\text{@SSP}})$ . The new thrust values  $(T^*)$  corresponding to these adjusted skin friction correction forces are then obtained by interpolation along the measured thrust vs tow force data (dashed line).

Shifting the focus from varying propeller speeds to different levels of wind assistance provides a clearer understanding of its role in supplementing conventional propulsion. By evaluating the vessel's hydrodynamic performance under varying wind assistance, we can assess its impact on resistance, propeller efficiency, rudder effectiveness, and overall power requirements. This approach helps optimize the balance between engine-driven propulsion and wind-generated thrust, offering a better understanding of the design and operation of wind-assisted ships.

A range of propeller RPMs was tested, covering both the ship's self-propulsion point and reduced propeller loading scenarios that simulate direct thrust contributions from wind propulsion. Figure 12 illustrates the relationship between the tow force coefficients and recorded shaft RPM across different rudder and leeway angles. The figure displays a nonlinear pattern where the tow force coefficient

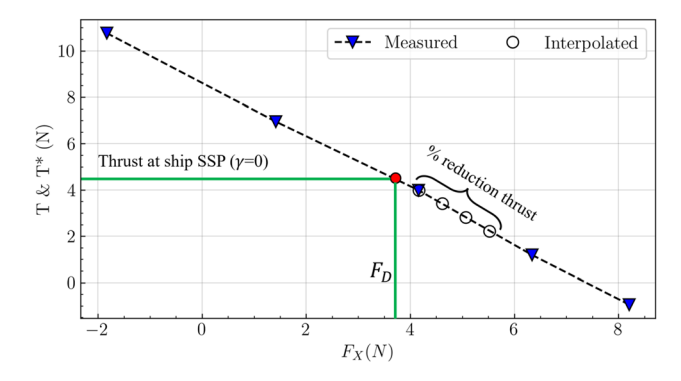
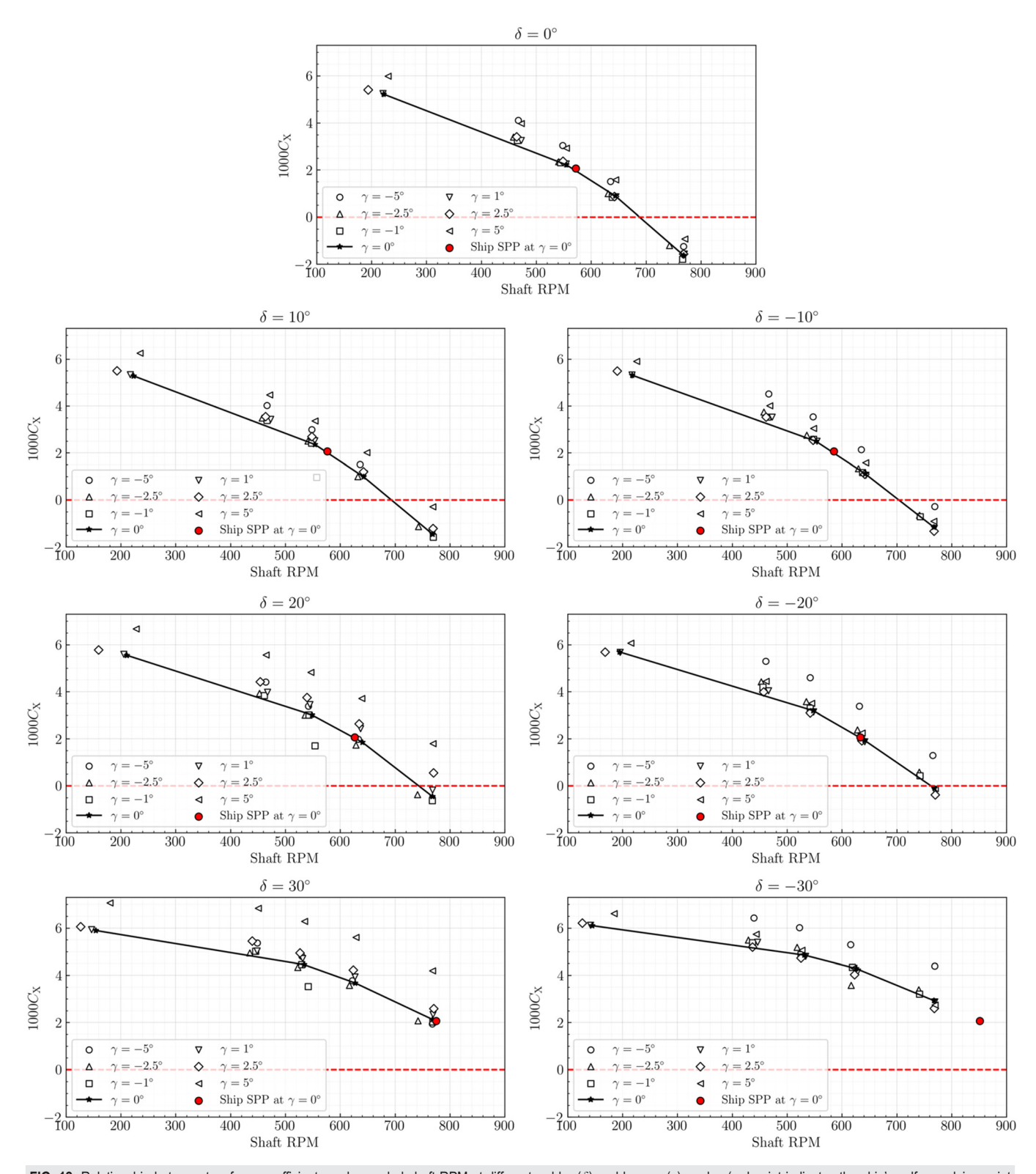


FIG. 11. Method for calculating different thrust loading using the thrust at the ship's self-propulsion point



**FIG. 12.** Relationship between tow force coefficients and recorded shaft RPM at different rudder ( $\delta$ ) and leeway ( $\gamma$ ) angles (red point indicates the ship's self-propulsion point at a zero-leeway angle).

decreases as the shaft RPM increases. The red point represents the ship's self-propulsion point with zero leeway and rudder angle, where the model scale tow force is equal to  $F_{\rm D}$ . The figure also highlights the variability of the recorded shaft RPM under different conditions, suggesting that propeller loading is sensitive to both rudder and leeway angles, as well as potential contributions from wind-assisted thrust, i.e., changes in propeller loading directly affected the achieved RPM.

Using the calculated  $F_{\rm D}$  value alongside spline interpolation of the measured data, we derived key metrics such as propeller thrust, torque, shaft RPM, side force, yaw moment, and rudder forces. These

results, specific to the ship's self-propulsion point, are denoted with an asterisk (\*) to distinguish them from the measured data discussed.

#### B. Hydrodynamic side forces

Figure 13 illustrates the side force coefficient at the ship's self-propulsion point ( $C_S^*$ ) under various percentages of thrust from the wind condition, across a range of leeway and rudder angles. The figure highlights how both rudder and leeway angles contribute to the total side force, demonstrating a clear interaction between these two variables. The plot shows near-symmetry around the  $0^\circ$  rudder angle,

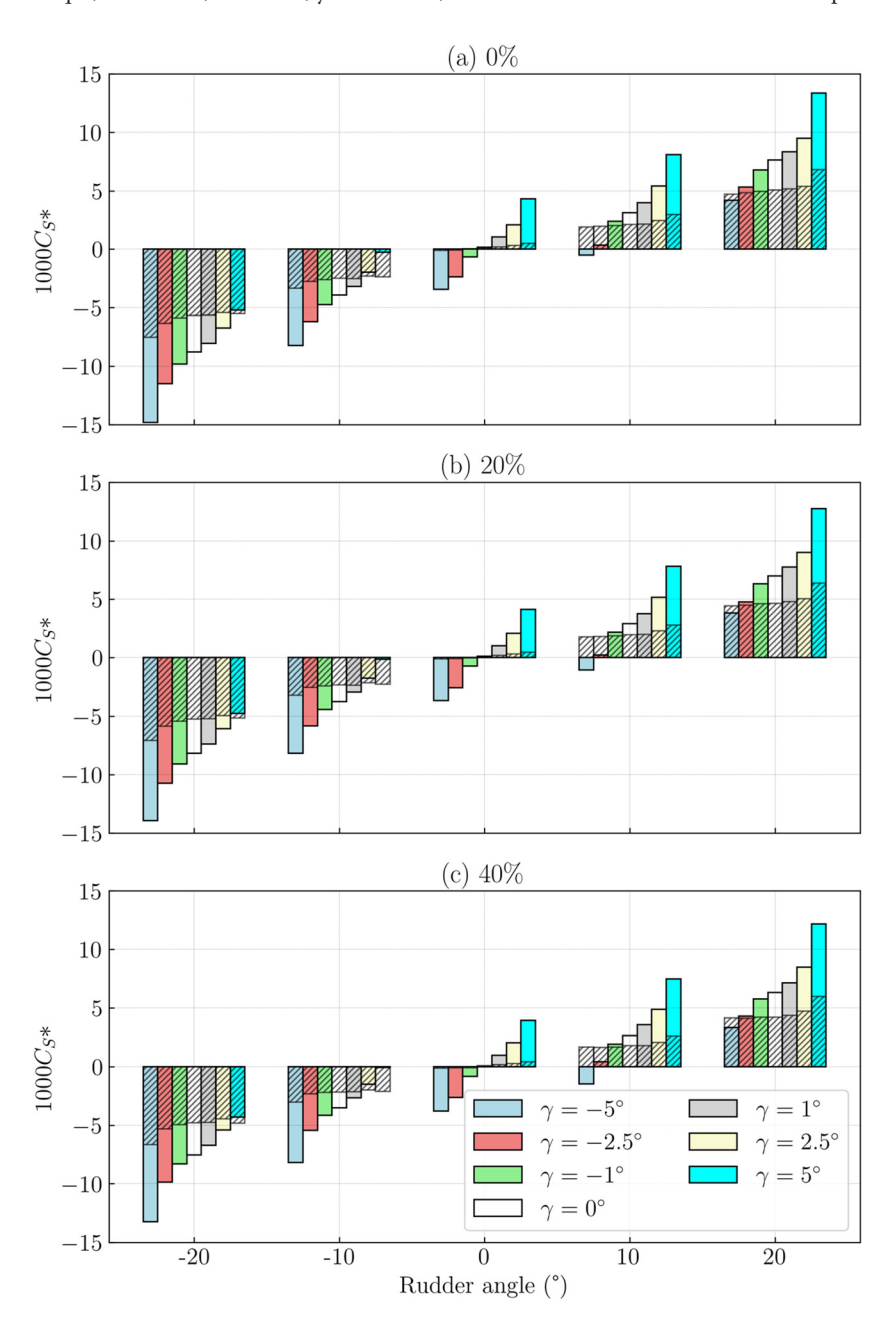


FIG. 13. Influence of combined rudder and leeway angles on the model's side force coefficient at different percentages of reduction thrust from wind conditions (hatched area represents the rudder's contribution to the total side force coefficient); (a) under 0% reduction thrust, (b) 20% reduction thrust, (c) 40% reduction thrust.

suggesting that the hull and rudder configuration maintain a balanced response to both port and starboard leeway angles. Notably, the rudder angle exerts a more substantial influence on the side force than the leeway angle. Figure 13 also presents the contribution the rudder side force makes to the total side force as hatched areas, allowing the relative contributions from the hull and rudder to be investigated. Importantly, the side force coefficients for both the rudder and the model were calculated using the same wetted surface area, allowing for the comparison of their respective contributions.

It is shown that the relationship between leeway angle and side force coefficient is nonlinear, particularly at high rudder angles, highlighting the complexity of ship behavior under varying conditions, as well as the effects of rudder stall and the influence of leeway angle on it. Even with a 0° rudder angle, the figure shows noticeable side forces due to leeway alone, indicating that the hull behaves as a lowaspect ratio foil and contributes to lateral forces without the rudder's input. Perhaps more interestingly, we can see that when a rudder angle (e.g., 20°) is applied at zero leeway angle (depicted by white bars), a significant proportion of the total side force (up to 66%) comes from the rudder indicating that the rudder significantly changes the flow around the stern of the hull. Therefore, it will be important to include the influence of the propeller and rudder on predictions of the hull's side force for accurate determination of the leeway angle. The impact of thrust reduction on total side force generation can also be assessed. For example, at a leeway angle of 2.5° and a rudder angle of 10°, a 10% change in total side force is observed between 0% and 40% wind conditions. Furthermore, at 40% thrust reduction, the side force increases by approximately 90% when the leeway angle is increased from 0° to +5°, at a constant rudder angle of 10°, clearly highlighting the strong influence of leeway on lateral force generation. In comparison, for the 0% wind-assisted case, the same change in leeway and rudder angles results in an increase in about 87% in side force.

The data shows that a thoughtful combination of rudder and leeway angles can be used to efficiently manage side forces, even in windassisted conditions. Careful rudder angle management can compensate for drift-induced side forces, providing greater control over the ship's course and reducing the need for additional propeller input. The figure clearly demonstrates the complex interactions between aero-hydro effects, showing how different rudder and leeway angles can be utilized to improve performance under various operational scenarios.

The side force generated by the hull C\*<sub>SH</sub> can be evaluated as the difference between the total side force coefficient (Cs) and the rudder's side force coefficient ( $C_{SR}^*$ ), where  $C_{SH}^* = C_S^* - C_{SR}^*$ . Figure 14 shows how the hull's side force is affected by both rudder and leeway angle. The rudder's impact on the hull's side force generation increases with the rudder angle, following an almost linear trend. Additionally, for negative rudder angles (e.g.,  $\delta = -10^{\circ}$  and  $-20^{\circ}$ ), the overall side force is negative, indicating a stronger force pushing the ship to one side. As the rudder angle becomes positive, the side force increases and becomes positive as well, meaning the rudder is generating a force that aligns with the direction of the leeway. This is especially pronounced at higher leeway angles, where rudder forces become a significant factor in complementing the natural drift of the hull. For  $\delta = 0^{\circ}$ , the rudder does not contribute much to the side force, which remains largely a function of the leeway angle. However, as the rudder angle increases to positive values  $\delta = 10^{\circ}$  and  $\delta = 20^{\circ}$ , the contribution of the rudder becomes more pronounced. This suggests that for greater rudder

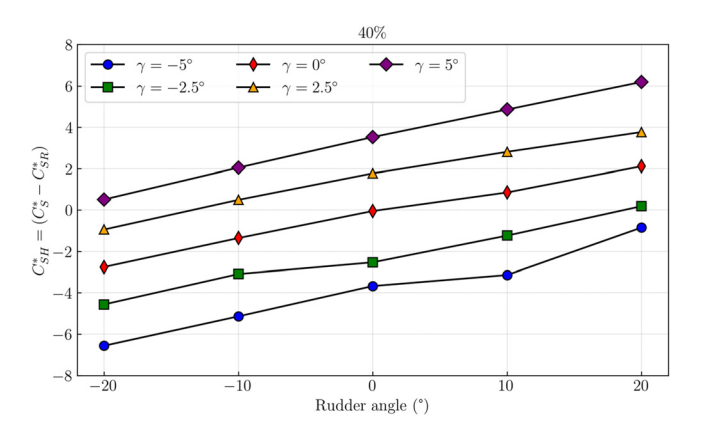


FIG. 14. Relationship between hull side force and rudder angle at different leeway angles and 40% reduction thrust from wind conditions.

angles, the rudder can be used effectively to control the side force generated by the hull, especially in conditions where higher leeway angles might naturally increase the side force due to wind. The almost linear relationship between rudder angle and C\*<sub>SH</sub> indicates that the rudder's influence grows steadily as the hull's leeway angle increases. However, the rate of increase in C\*<sub>SH</sub> is dependent on the rudder angle, with larger rudder angles generating a more substantial change in the side force coefficient. This behavior is crucial for understanding how rudder adjustments can be used to counteract the effects of leeway, particularly in wind-assisted ships where side forces from both aerohydrodynamic sources must be balanced to maintain course stability.

# C. Hydrodynamic yaw moments

Figure 15 illustrates the impact of leeway and rudder angle on the total yaw moment coefficient (CN) for two different levels of wind propulsion. The plot demonstrates that both leeway angle and rudder angle have a significant impact on the hydrodynamic yaw moment generated. The inset subplot in Fig. 15 focuses on the yaw moment at  $\pm 5^{\circ}$  leeway angles across a range of rudder angles, further illustrating the dynamic interplay between rudder and leeway angles. The lines in this subplot intersect the zero-yaw moment axis at specific rudder angles, marked with red points. These intersections indicate the required rudder angle to counteract the hydrodynamic yaw moment generated by the corresponding leeway angle, effectively balancing the ship's yaw. This figure also suggests that rudder inputs must be carefully adjusted to balance yaw moments, especially in high wind conditions where the vessel may be subject to large aerodynamic forces.

The rudder's moment (C\*NR) contribution to the total yaw moment coefficient  $(C_N^*)$  is presented in Fig. 15 as hatched areas. The rudder yaw moment at the total yaw pivot point is determined using the measured rudder forces at the rudder stock ( $F_{xR}$  and  $F_{vR}$ ), multiplied by a lever arm as shown in Fig. 1. As expected, the rudder's contribution varies significantly with rudder angle but also to a lesser extent with leeway angle, again highlighting the interaction between the hull and the rudder. At large negative rudder angles ( $-20^{\circ}$ ), the rudder produces a substantial positive yaw moment, accounting for approximately half of the total yaw moment (at  $\gamma = 5^{\circ}$ ). As the rudder angle increases toward positive values, the rudder's contribution gradually decreases and becomes negative at positive rudder angles,

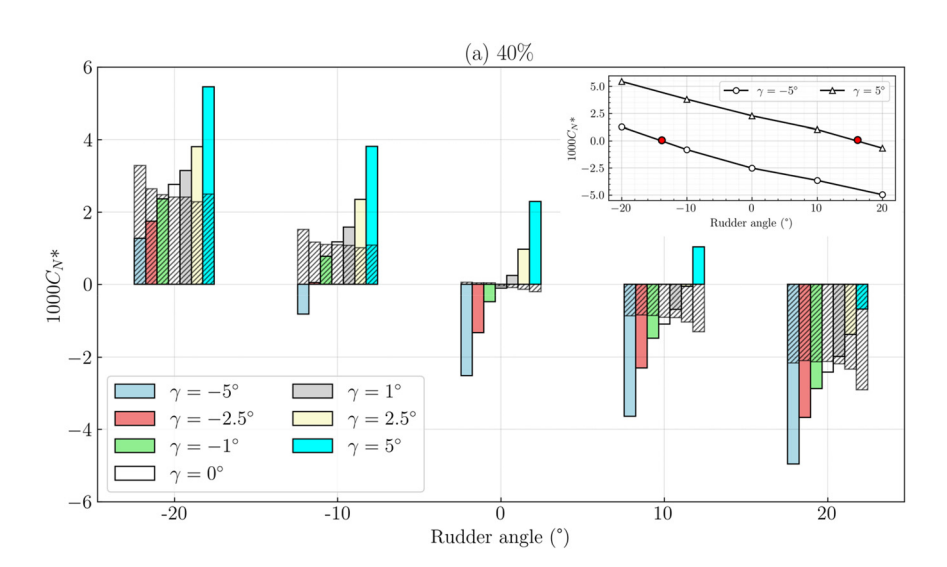
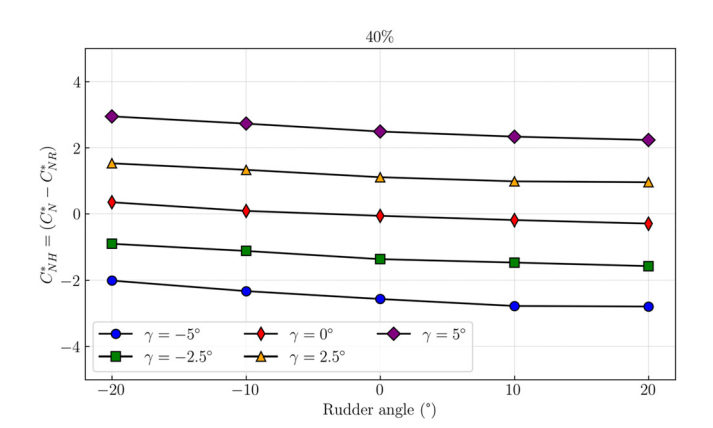


FIG. 15. Effect of rudder and leeway angle on the model's yaw moment coefficient at 40% reduction thrust from wind conditions; hatched area represents the rudder's contribution to the total yaw moment coefficient (note: the red point in the subplot shows the required rudder angle to balance the yaw moment).

particularly evident at +20°. This trend demonstrates the asymmetric nature of the rudder's effectiveness across different leeway angles. As expected, at small rudder angles near 0°, the rudder's contribution to the total yaw moment is minimal. The hatched areas also reveal that the rudder's effectiveness in generating yaw moment is more pronounced at extreme rudder angles (±20°) compared to moderate angles, indicating a nonlinear relationship between rudder angle and its contribution to the total yaw moment. In addition, it is shown that at 40% thrust reduction, the magnitude of the yaw moment increases by 54% when the leeway angle is increased from  $0^{\circ}$  to  $+5^{\circ}$ , at a constant rudder angle of 10°, compared to a 61% increase for no wind scenario. The presence of leeway angles appears to modify the rudder's contribution, though the hatched areas maintain a consistent pattern across different leeway angles, suggesting that the fundamental mechanism of rudder-induced yaw moment remains similar despite varying drift conditions.

In addition, the hull's yaw moment is calculated as  $C_{NH}^* = C_N^* - C_{NR}^*$ , where  $C_N^*$  represents the total yaw moment and  $C_{NR}^*$  is the rudder's contribution to the total yaw moment and is presented



**FIG. 16.** Relationship between hull yaw moment and rudder angle at different leeway angles and 40% reduction thrust from wind conditions.

in Fig. 16. As expected, the leeway angle has the biggest impact on the yaw moment generated by the hull. Although the rudder angle does have a small impact on the hull's yaw moment, this effect is much smaller than for the hull's side force.

The relationship between rudder angle and hull yaw moment  $(C_{NH}^*)$  demonstrates an almost linear trend. It is shown that the positive leeway angles generate positive hull moments and negative leeway angles produce negative moments. At zero leeway angle, the hull yaw moment remains close to neutral, aligning with theoretical expectations. The magnitude of the hull yaw moment increases substantially with increasing leeway angle. A notable characteristic of the hull yaw moment is its relative insensitivity to rudder angle variations, as evidenced by the nearly horizontal lines for each leeway angle condition. This independence from rudder angle suggests the hull's contribution to the overall yaw moment is primarily governed by the leeway angle. The observed symmetry between positive and negative leeway angles further indicates the consistent hydrodynamic behavior of the hull.

Figure 17 explores the rudder angles required to balance the hydrodynamic-induced yaw moments for various leeway angles and different percentages of thrust from the wind. It is evident that higher wind percentages generally require slightly larger rudder angles to

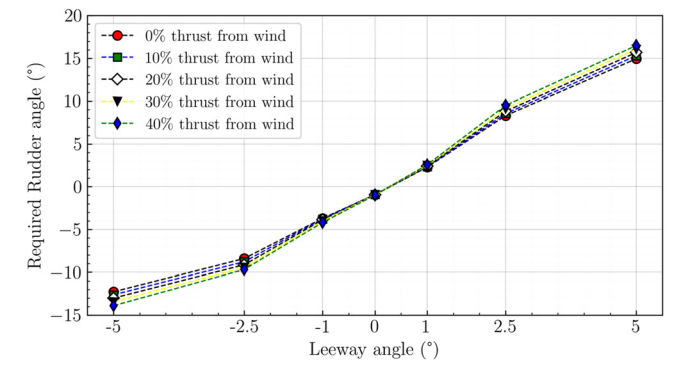


FIG. 17. Relationship between required rudder angle and leeway angle at various wind conditions

maintain equilibrium, especially at more extreme leeway angles. This can be explained by the reduced flow velocity over the rudder for lower propeller loadings. The relationship between the leeway angle and the corresponding rudder angle appears to be nearly linear. While higher wind assistance levels lead to an increase in the required rudder angle, the difference between them remains relatively modest. This indicates that as the proportion of wind propulsion increases, the required rudder angle will be driven by the leeway angle required to generate side force rather than the propeller rudder interaction. From an operational perspective, this emphasizes the potential requirement for large rudder angles to maintain a course, for example, for a 2.5° leeway angle, approximately 10° of rudder angle is required to balance the hydrodynamic yaw moment. Therefore, the positioning of wind propulsion devices should be carefully optimized to minimize the rudder angles required for balance, enhancing overall ship performance. In general sailing conditions, the performance of a vessel is optimized when the aerodynamic and the hydrodynamic center of effort are positioned relatively close to each other. Similar to what is observed in traditional yacht design, this close alignment of force centers creates a more balanced and efficient sailing system that requires less compensatory steering and allows the vessel to maintain higher speeds with greater stability. This is discussed in the next subsection.

#### D. Discussion of WAS performance

The performance of wind-assisted vessels and the hydrodynamic interactions between rudder angle, propeller loading, and leeway angle are discussed in this section. Wind-assisted vessels generate large aerodynamic side forces that must be balanced by hydrodynamic side forces to maintain course. In practice, the hull's drift and rudder angle create the compensating side force, but they also cause extra drag. Thus, a key performance metric is the ratio of side force to longitudinal force ( $C_S/C_X$ ), analogous to a "lift-to-drag" ratio in aerodynamics. A higher  $C_S/C_X$  means the ship produces more lateral force per unit drag, which is desirable for efficient course-keeping and turning under wind propulsion.

Figure 18 illustrates the relationship between rudder angle and the total side-force-to-tow-force ratio  $(C_{\rm S}/C_{\rm X})$  at different leeway angles and under varying propeller loading conditions. The results reveal that without propeller operation, the rudder exhibits negligible effectiveness, with  $C_{\rm S}/C_{\rm X}$  values remaining close to zero for low rudder angle adjustments. This demonstrates the rudder's limited hydrodynamic influence in the absence of propeller wake interaction. In contrast, powered conditions show pronounced responses, with the magnitude of  $C_{\rm S}/C_{\rm X}$  increasing proportionally with propeller RPM. This phenomenon can be attributed to the accelerated flow over the rudder surface created by propeller action, enhancing pressure differentials and therefore force generation.

In addition, the behavior patterns exhibit notable variation across different leeway angles. At zero leeway, the  $C_S/C_X$  curves display approximate symmetry about the origin, whereas introducing leeway produces distinct asymmetric responses. This asymmetry holds particular significance for wind-assisted ships, as it reflects how rudder effectiveness fluctuates depending on whether the vessel needs to counteract or complement the leeway forces generated by wind assistance systems. Moreover, as the rudder angle becomes larger, the ship generates more side force, and this increase is greater than the increase in drag. This is why the  $C_S/C_X$  values go up with rudder angle. It shows

that the rudder is working efficiently at these angles, creating a strong side force without adding too much drag. Higher propeller RPM uniformly augments the  $C_{\rm S}/C_{\rm X}$  curves across all measured angles, demonstrating that increased propulsion flow substantially enhances the rudder's hydrodynamic performance. The accelerated flow effectively amplifies the rudder's capacity to generate lateral force with relatively minimal additional drag penalty, thereby improving the vessel's maneuverability characteristics and course-keeping capabilities in wind-assisted operations.

The analysis of the rudder lift-to-drag ratio  $C_{\rm SR}/C_{\rm DR}$  across different propeller loading conditions, Figs. 9 and 10 indicate that the ratio remains largely consistent regardless of whether the propeller is active or not. This suggests that the rudder's aerodynamic efficiency is relatively unaffected by the propeller-induced flow, and its performance in generating side force with respect to drag remains stable across propulsion conditions. <sup>50</sup>

Following the approach commonly used in the performance analysis of sailing yachts,<sup>51</sup> the relationship between side force generation and the associated increase in resistance is examined to assess the hydrodynamic efficiency of the hull under leeway. Based on the liftingline theory of wings,  $^{43,\dot{5}2}$  the linear relationship  $C_X=\frac{1}{\pi AR_{\rm eff}}C_S^2+C_{X0}$ allows us to estimate the effective aspect ratio AR<sub>eff</sub> of the hull and appendages, essentially a measure of how efficiently the hull generates side force with minimal drag penalty. Figure 19 presents this relationship at various propeller RPMs, all measured at zero rudder angle and varying leeway, with linear fits capturing the trend. The slope of each line corresponds to the induced drag component due to side force, meaning flatter slopes (lower induced drag) indicate more hydrodynamically efficient configurations. All lines remain roughly linear and nearly parallel, which implies the induced-drag coefficient (and thus AR<sub>eff</sub>) is little changed by turning the propeller on; the hull's response to side force is similar in each case. In contrast, the vertical offsets shift dramatically with RPM: higher propeller speed drives the intercept C<sub>X0</sub> downward (the highest RPM even gives a negative intercept, meaning the propeller's thrust overcomes the hull's drag). In other words, increasing RPM greatly reduces the baseline resistance (net drag), while the cost of additional side force (the slope) only changes it modestly. Any small change in slope could hint at propeller-wake effects altering the flow around the hull or keel (slightly changing the apparent aspect ratio).

Figure 20 presents a critical analysis of hydrodynamic force generation efficiency through the relationship between lift-curve slopes and propeller thrust loading. The plot distinguishes between total vessel side force (solid line) and isolated rudder lift (dashed line), with unpropelled conditions marked separately at the origin. These results present the average lift-curve slope ( $dC_S/d\delta$ )—the derivative of sideforce coefficient with respect to rudder angle—against the propeller thrust loading ( $K_T/J^2$ ). The average slope values are obtained by fitting linear side-force vs rudder-angle curves (Figs. 7 and 10) at each fixed leeway angle in the range of  $\pm 2.5^{\circ}$  (with rudder angles from  $-20^{\circ}$  to  $+20^{\circ}$ ), and then averaging the slopes across these leeway angles.

The data reveal a pronounced linear correlation between lift generation capability and thrust loading, with both total side force and rudder-specific lift slopes increasing systematically as thrust loading intensifies. This linear relationship demonstrates how propeller-induced flow enhances the hydrodynamic effectiveness of both the hull-propeller-rudder system and the rudder in isolation. Notably, the

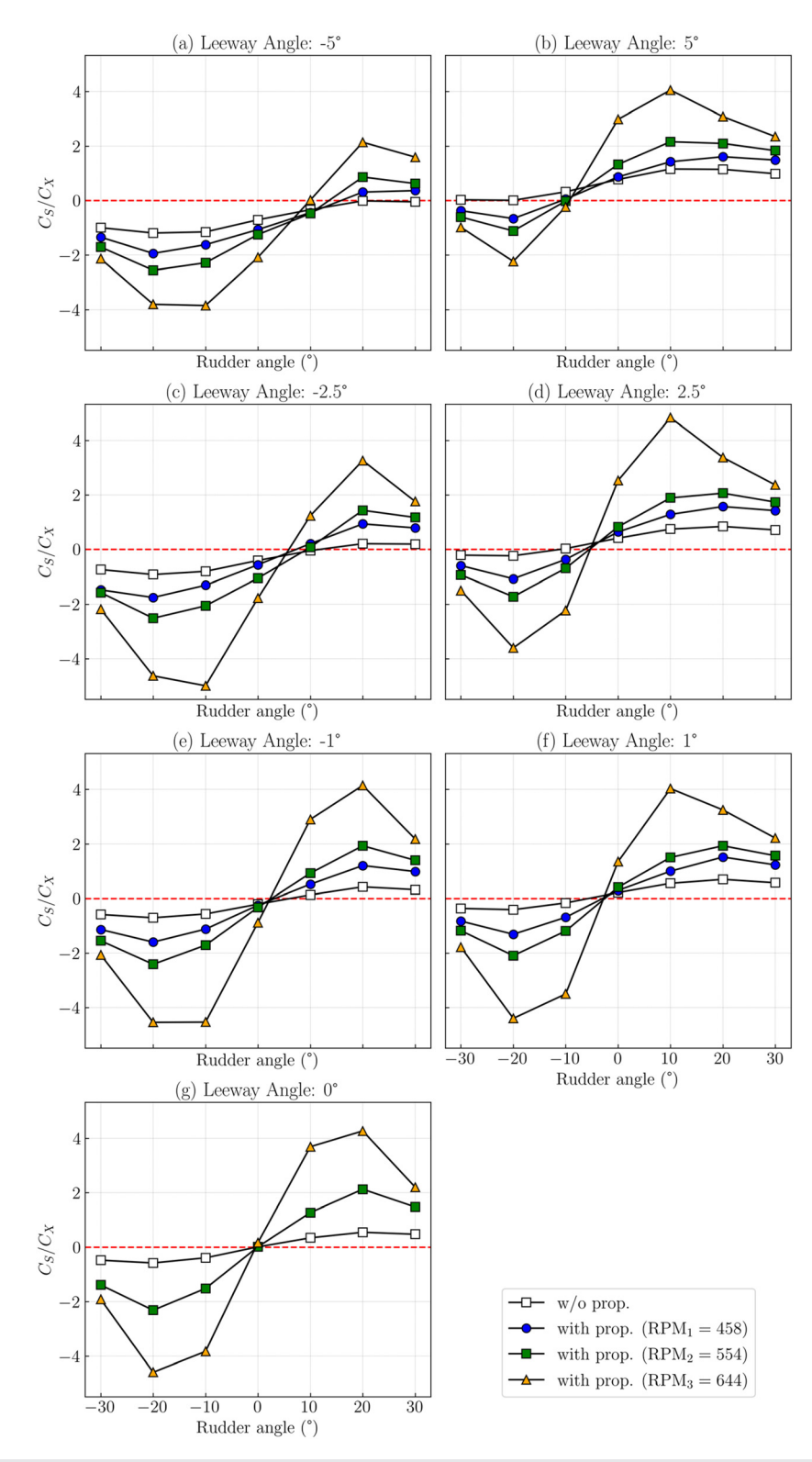
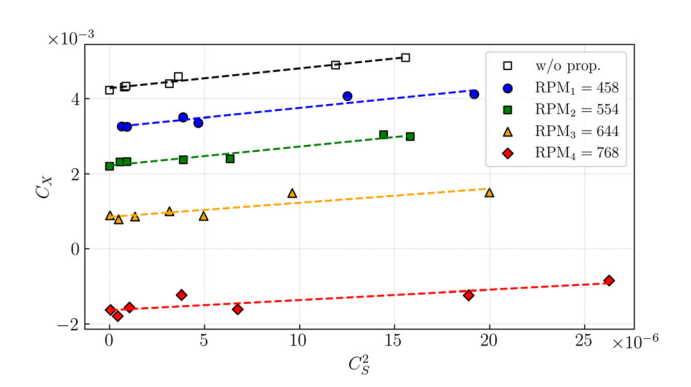


FIG. 18. Rudder effectiveness represented by total side-force-to-tow-force ratio (C<sub>S</sub>/C<sub>X</sub>) as a function of rudder angle at different leeway angles and propeller RPMs, including the comparison with non-propelled hull (w/o prop.).



**FIG. 19.** Relationship between total tow force coefficient  $(C_X)$  and squared side force coefficient  $(C_S^2)$  at zero rudder angle for various leeway angles and propeller loading conditions.

total side force slope exhibits a steeper gradient compared to the rudder alone, indicating substantial hull contribution to lateral force generation under propeller influence. The unpropelled case (at zero advance ratio) establishes a baseline reference point for passive hydrodynamic performance. Further analysis reveals that while lift-curve slopes remain relatively consistent at modest leeway angles, they demonstrate progressive increases at more extreme leeway angles (exceeding  $\pm 2.5^{\circ}$ ). This nonlinear behavior at higher leeway angles suggests complex flow interactions affecting the hull's hydrodynamic characteristics under combined propulsion and lateral drift conditions.

An essential parameter in the analysis of wind-assisted ships is the center of effort (CoE) of the hydrodynamic side force distribution, which plays a critical role in assessing a vessel's maneuverability and course-keeping capabilities. In wind-assisted propulsion, the ship hull generates lateral force as a response to the aerodynamic side force induced by the wind propulsion system. This is achieved by sailing at a leeway angle, effectively turning the hull into a lifting surface. When a vessel sails steadily at such an angle, it experiences a significant hydrodynamic yaw moment, commonly referred to as the Munk moment, which acts to rotate the vessel broadside to the incoming flow. This destabilizing effect is characteristic of slender bodies exposed to oblique flows, where the asymmetric pressure field along the hull naturally generates a restoring torque opposing directional stability.

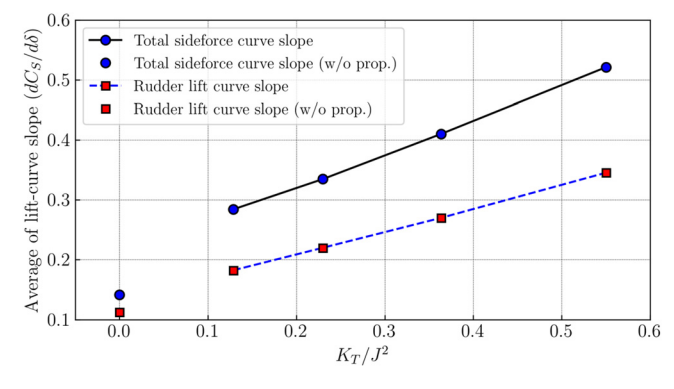


**FIG. 20.** Variation of the average of lift-curve slope (dC<sub>S</sub>/d $\delta$ ) with propeller thrust loading (K<sub>T</sub>/J<sup>2</sup>).

This quantity represents the effective lever arm of the side force distribution and directly influences the amount of rudder input required to counteract the yawing moment for a given lateral force. It typically lies forward of midship due to the nature of flow development along the hull. Typically, this center is positioned substantially forward of midship. Studies on various vessel configurations have demonstrated that the center of lateral resistance can vary from 0.44 to 0.54 ship lengths ahead of midship for moderate drift angles,<sup>54</sup> with some extreme cases positioning it a full ship length ahead of midship. Hull appendages like bilge keels can shift this center closer to the bow, although rarely behind it, significantly affecting directional stability and control requirements. <sup>52,55</sup>

The CoE ( $CoE = M_z/F_v$ ) is calculated by dividing the hydrodynamic yaw moment by the total side force, with measurements transferred to the ship axis system and positions normalized by the ship length between perpendiculars. Figure 21 presents these normalized CoE measurements under varying conditions. In Fig. 21(a), the CoE variation across different leeway angles at zero rudder angle demonstrates that the center of effort progressively shifts forward as leeway angle increases, with values consistently above 0.8 (where zero represents the aft perpendicular). The data reveal a nearly symmetrical pattern between positive and negative leeway angles, though with slight asymmetries attributable to propeller rotation effects. Figure 21(b) expands this analysis by examining CoE position at fixed leeway angles of  $\pm 5^{\circ}$  across various rudder angles. The results clearly demonstrate how rudder angle systematically shifts the center of effort toward midship, effectively redistributing the lateral force generation. This repositioning effect is pronounced at both positive and negative leeway angles. Additionally, the figure reveals how propeller loading influences CoE positioning, with different RPM settings creating distinct patterns. Notably, the unpropelled condition (white squares) maintains relatively high CoE values across all rudder angles, while propelled conditions show greater sensitivity to rudder angle. This behavior illustrates the complex interaction between propeller-induced flow, rudder effectiveness, and overall lateral force distribution that must be carefully considered when designing control systems for wind-assisted vessels.

#### VI. CONCLUSIONS

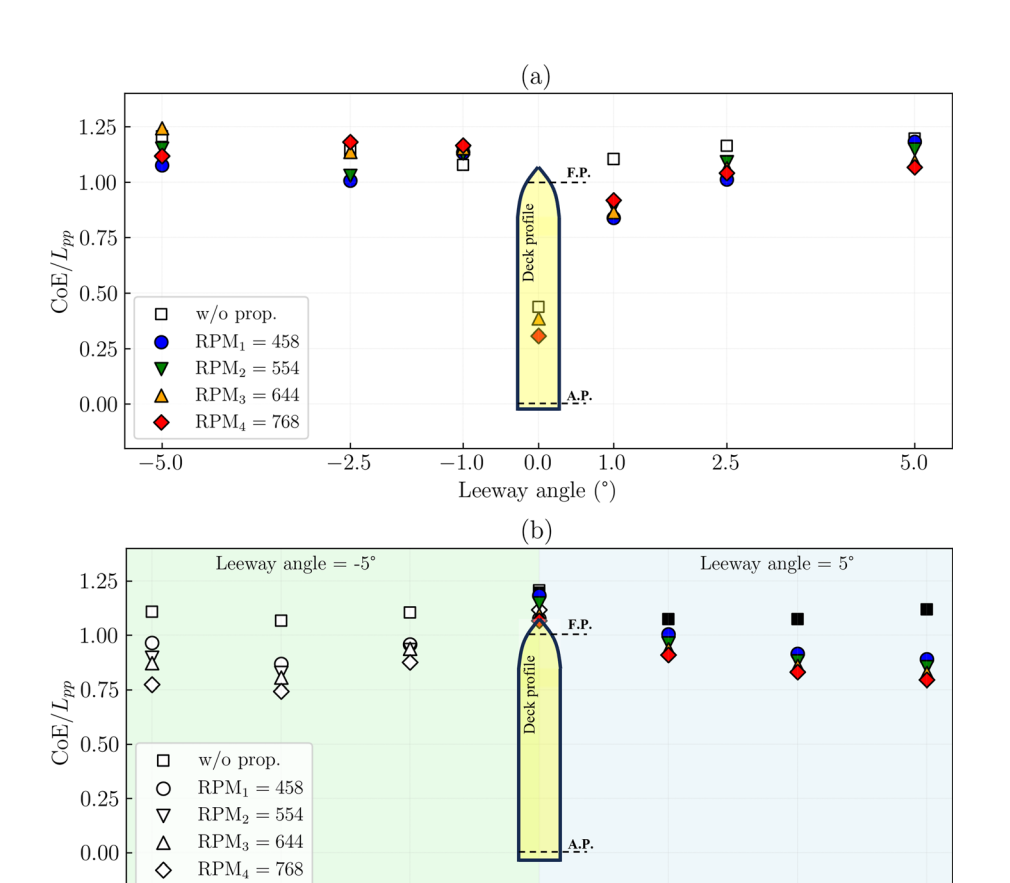
The effects of leeway and rudder angles on the hydrodynamic forces acting on a containership are examined. A series of resistance, non-propelled, and self-propelled captive tests was carried out on a single-screw KCS model to assess the interactions between hull, rudder, and propeller. The results were presented as measured data and at the ship's self-propulsion point. The total tow force coefficient of the model was found to increase with both rudder angle magnitude and leeway angle, with the effect being more pronounced at negative leeway angles which is due to the propeller rotation direction and its influence on flow straightening driven by the effective propeller thrust loading.

Key conclusions from the study are as follows:

(i) The rudder's contribution to overall side force increases significantly with leeway angle, following a nearly linear trend, underscoring its critical role in counteracting wind-induced forces. As rudder angles become larger, especially in combination with higher leeway angles, their effect on yaw

30

-20



0

Rudder angle (°)

10

20

30

**FIG. 21.** Center of effort presented at (a) different leeway angle and zero rudder angle; (b)  $\pm 5^{\circ}$  leeway angle and a range of rudder angles.

moment correction becomes increasingly pronounced until stall occurs.

-10

- (ii) Larger rudder angles are required to balance the yaw moments generated by increased leeway angles and wind propulsion. Wind assistance amplifies these yawing moments, making precise rudder control essential for maintaining heading. The analysis of yaw moment coefficients under varying wind-assist levels highlights the complex interaction between rudder and leeway angles and provides insights into steering demands for a wide range of ship types and wind-assist configurations.
- (iii) The force ratio between side force and tow force  $(C_S/C_X)$  was investigated, demonstrating that propeller-induced flow enhances rudder effectiveness and promotes favorable hydrodynamic force generation.
- (iv) The expected linear relationship was confirmed between total resistance and the square of the side force for a low aspect control surface, validating predictions from liftingline theory and providing a useful metric for evaluating hydrodynamic efficiency under different operating scenarios.
- (v) Analysis of the rudder's rate of change of side force with rudder angle showed that increasing propeller thrust loading systematically improves the vessel's steering response,

- offering valuable guidance for designing control systems for wind-assisted ships.
- (vi) The hull center of effort analysis demonstrated how rudder action redistributes lateral forces forward along the hull, helping manage yaw moments and achieve balance between aerodynamic and hydrodynamic forces.

Overall, these findings establish an integrated approach to hull-propeller-rudder optimization for wind-assisted vessels, where balancing propulsive efficiency and course-keeping capability is essential. By leveraging these hydrodynamic relationships, designers can develop future wind-assisted ships that more effectively harness renewable energy while maintaining directional stability and maneuverability across a wide range of operating conditions. Careful adjustment of rudder and leeway angles, supported by robust hull and rudder designs, can unlock significant energy savings, reduce fuel consumption, and lower emissions. These insights contribute to the ongoing optimization of wind-assisted propulsion integration in modern shipping operations.

# **ACKNOWLEDGMENTS**

This work was conducted as part of the Winds of Change Clean Maritime Demonstration project funded by UKShore and Innovate UK. The authors acknowledge the staff at the Wolfson Unit MTIA, Dickon Buckland and Etienne Gauvain, for their crucial role greatly contributed to the preparation of our experiments. The author further expresses gratitude to the dedicated staff at the Boldrewood Towing Tank at the University of Southampton for their invaluable support throughout this experimental study.

# AUTHOR DECLARATIONS Conflict of Interest

The authors have no conflicts to disclose.

#### **Author Contributions**

Saeed Hosseinzadeh: Conceptualization (equal); Data curation (equal); Formal analysis (equal); Investigation (equal); Methodology (equal); Validation (equal); Writing – original draft (equal); Writing – review & editing (equal). Dominic Hudson: Conceptualization (equal); Supervision (equal); Writing – review & editing (equal). Stephen R. Turnock: Conceptualization (equal); Investigation (equal); Software (equal); Supervision (equal); Writing – review & editing (equal). Martyn Prince: Investigation (equal); Writing – review & editing (equal). Joseph Banks: Conceptualization (equal); Funding acquisition (equal); Investigation (equal); Project administration (equal); Supervision (equal); Writing – review & editing (equal).

#### DATA AVAILABILITY

Part of the dataset from the self-propulsion experiments is available in the University of Southampton Institutional Repository, <sup>56</sup> with detailed usage instructions in Hosseinzade *et al.*<sup>37</sup> The rest of data will be provided upon request.

### REFERENCES

- <sup>1</sup>International Maritime Organization, Marine Environment Protection Committee, "IMO, IMO strategy on reduction of GHG emissions from ships," Technical Report (International Maritime Organization, Marine Environment Protection Committee, 2023).
- <sup>2</sup>M. Fluck, A. Wright, D. Morris, M. Prince, and J. Elliott, "Progress in development and design of Dynarigs for commercial ships," in *SNAME Chesapeake Sailing Yacht Symposium* (SNAME, 2022), p. D011S002R001.
- <sup>3</sup>Q. Zeng, X. Lyu, W. Cai, L. Zhang, and J. Xu, "Influence of wind gradient and ground effect on the aerodynamic forces of a Dynarig sail at large heeling angles," Ocean Eng. 312, 119069 (2024).
- <sup>4</sup>W. Formosa, T. Sant, C. D. Muscat-Fenech, and M. Figari, "Wind-assisted ship propulsion of a series 60 ship using a static kite sail," J. Mar. Sci. Eng. 11, 117 (2023).
- <sup>5</sup>R. Lu and J. W. Ringsberg, "Ship energy performance study of three windassisted ship propulsion technologies including a parametric study of the Flettner rotor technology," Ships Offshore Struct. 15, 249 (2020).
- <sup>6</sup>V. Vigna and M. Figari, "Wind-assisted ship propulsion: Matching flettner rotors with diesel engines and controllable pitch propellers," J. Mar. Sci. Eng. 11, 1072 (2023).
- <sup>7</sup>K. Ouchi, K. Uzawa, and A. Kanai, "Huge hard wing sails for the propulsor of next generation sailing vessel," in The Second International Symposium on Marine Propulsors, Hamburg, Germany, 2011.
- <sup>8</sup>C. Li, H. M. Wang, and P. T. Sun, "Study on the influence of gradient wind on the aerodynamic characteristics of a two-element wingsail for ship-assisted propulsion," J. Mar. Sci. Eng. 11, 134 (2023).
- <sup>9</sup>M. Petković, M. Zubčić, M. Krčum, and I. Pavić, "Wind assisted ship propulsion technologies—Can they help in emissions reduction?," NAŠE MORE **68**, 102 (2021).
- <sup>10</sup>L. Khan, J. Macklin, B. Peck, O. Morton, and J.-B. R. G. Souppez, A Review of Wind-Assisted Ship Propulsion for Sustainable Commercial Shipping: Latest Developments and Future Stakes (Royal Institution of Naval Architects, 2021).

- <sup>11</sup>A. Molland and G. Hawksley, "An investigation of propeller performance and machinery applications in wind assisted ships," J. Wind Eng. Ind Aerodyn. 20, 143 (1985).
- <sup>12</sup>J. Wellicome, "Some comments on the relative merits of various wind propulsion devices," J. Wind Eng. Ind Aerodyn. 20, 111 (1985).
- <sup>13</sup>C. Satchwell, "Aerodynamic design of marine aerofoils," J. Wind Eng. Ind Aerodyn. 20, 1 (1985).
- <sup>14</sup>J. Väinämö, "Operational experiences and results from the first reference installation from Nov-2014, Roro-Ship Estraden (9700 Dwt)," in 24th International HISWA Symposium on Yacht Design and Yacht Construction, Amsterdam, The Netherlands, 2016.
- <sup>15</sup>H. Lee, Y. Jo, D.-J. Lee, and S. Choi, "Surrogate model based design optimization of multiple wing sails considering flow interaction effect," Ocean Eng. 121, 422 (2016).
- 16 K. Ouchi, K. Uzawa, A. Kanai, and M. Katori, "Wind challenger' the next generation hybrid sailing vessel," in *The Third International Symposium on Marine Propulsors, Launceston, Tasmania, Australia* (Australian Maritime College, 2013), pp. 562–567.
- <sup>17</sup>F. Tillig and J. W. Ringsberg, "Design, operation and analysis of wind-assisted cargo ships," Ocean Eng. 211, 107603 (2020).
- <sup>18</sup>N. R. Ammar and I. S. Seddiek, "Wind assisted propulsion system onboard ships: Case study Flettner rotors," Ships Offshore Struct. 17, 1616 (2022).
- <sup>19</sup>E. Lindstad, T. Stokke, A. Alteskjaer, H. Borgen, and I. Sandaas, "Ship of the future—A slender dry-bulker with wind assisted propulsion," Marit. Transp. Res. 3, 100055 (2022).
- <sup>20</sup> J. Mason, A. Larkin, S. Bullock, N. Van Der Kolk, and J. F. Broderick, "Quantifying voyage optimisation with wind propulsion for short-term CO<sub>2</sub> mitigation in shipping," Ocean Eng. 289, 116065 (2023).
- <sup>21</sup>T. Plessas and A. Papanikolaou, "Optimization of ship design for the effect of wind propulsion," in *Presented at the 15th International Marine Design Conference* (IMDC, 2024).
- <sup>22</sup>M. H. Arabnejad, F. Thies, H.-D. Yao, and J. W. Ringsberg, "Zero-emission propulsion system featuring, Flettner rotors, batteries and fuel cells, for a merchant ship," Ocean Eng. 310, 118618 (2024).
- <sup>23</sup>I. M. Viola, M. Sacher, J. Xu, and F. Wang, "A numerical method for the design of ships with wind-assisted propulsion," Ocean Eng. 105, 33 (2015).
- <sup>24</sup>F. Tillig, J. W. Ringsberg, W. Mao, and B. Ramne, "Analysis of uncertainties in the prediction of ships' fuel consumption—From early design to operation conditions," Ships Offshore Struct. 13, 13 (2018).
- <sup>25</sup>N. Van der Kolk, G. Bordogna, J. C. Mason, P. Desprairies, and A. Vrijdag, "Case study: Wind-assisted ship propulsion performance prediction, routing, and economic modelling," in *International Conference Power & Propulsion Alternatives for Ships* (The Royal Institution of Naval Architects, 2019).
- <sup>26</sup>J. V. Kramer and S. Steen, "Simplified test program for hydrodynamic CFD simulations of wind-powered cargo ships," Ocean Eng. 244, 110297 (2022).
- <sup>27</sup>J. A. Kramer, S. Steen, and L. Savio, "Drift forces—Wingsails vs. Flettner rotors," in Proceedings of the International Conference on High Performance Marine Vehicles, Cortona, Italy (Technische Universität Hamburg, 2016), pp. 17–19.
- <sup>28</sup>J. A. Kramer, S. Steen, and L. Savio, "Experimental study of the effect of drift angle on a ship-like foil with varying aspect ratio and bottom edge shape," Ocean Eng. 121, 530 (2016).
- <sup>29</sup>S. Turnock, S. Hosseinzadeh, Y. Zhang, J. Bowker, D. Buckland, M. Gregory, and N. Townsend, "Hull-propeller-rudder interactions: Time-accurate data of a scaled model ship in waves," Ocean Eng. 312, 119258 (2024).
- 30 S. Hosseinzadeh, D. Hudson, S. Turnock, M. Prince, and J. Banks, "Experimental investigation of the impact of leeway and rudder angles on the yaw moment balance for wind-propelled ships," in *Wind Propulsion Conference* (Royal Institution of Naval Architects, 2024).
- <sup>31</sup>Y. Zhang, S. Hosseinzadeh, J. Banks, D. Hudson, and S. Turnock, *Influence of Leeway on Hull-Propeller-Rudder Interaction Using CFD Methods* (Norwegian University of Science and Technology, 2023).
- 32Y. Zhang, H. R. Díaz-Ojeda, B. Windén, D. Hudson, and S. Turnock, "A numerical study of drift angle effect on hydrodynamic performance of a fully appended container ship in head waves," Ocean Eng. 313, 119343 (2024).
- <sup>53</sup>Y. Zhang, B. Windén, H. R. D. Ojeda, D. Hudson, and S. Turnock, "Influence of drift angle on the propulsive efficiency of a fully appended container ship (KCS) using Computational Fluid Dynamics," Ocean Eng. 292, 116537 (2024).

- <sup>34</sup>G. Bordogna, S. Muggiasca, S. Giappino, M. Belloli, J. Keuning, R. Huijsmans, and A. Van't Veer, "Experiments on a Flettner rotor at critical and supercritical Reynolds numbers," J. Wind Eng. Ind. Aerodyn. 188, 19 (2019).
- 35 T. Sauder and S. A. Alterskjaer, "Hydrodynamic testing of wind-assisted cargo ships using a cyber-physical method," Ocean Eng. 243, 110206 (2022).
- <sup>36</sup>B. Malas, L. Creasey, D. Buckland, and S. R. Turnock, "Design, development and commissioning of the Boldrewood towing tank-A decade of endeavour," Int. J. Marit. Eng. 165, A255-A271 (2024).
- <sup>37</sup>S. Hosseinzadeh, S. Turnock, H. Lee, and R. Olvera, "Experimental dataset of a model-scale ship in calm water and waves," Data Brief 58, 111257 (2025).
- <sup>38</sup>T. Hino, F. Stern, L. Larsson, M. Visonneau, N. Hirata, and J. Kim, *Numerical* Ship Hydrodynamics: An Assessment of the Tokyo 2015 Workshop (Springer Nature, 2020).
- <sup>39</sup>S. K. Mitra, Digital Signal Processing: A Computer-Based Approach (McGraw-Hill Higher Education, 2001).
- <sup>40</sup>ITTC, Recommended Procedures and Guidelines: General Guideline for Uncertainty Analysis in Resistance Tests (ITTC, 2021).
- <sup>41</sup>C. E. Badoe, A. B. Phillips, and S. R. Turnock, "Influence of drift angle on the computation of hull-propeller-rudder interaction," Ocean Eng. 103, 64 (2015).

  42 A. F. Molland, S. R. Turnock, and D. A. Hudson, Ship Resistance and
- Propulsion (Cambridge University Press, 2017).
- <sup>43</sup>A. F. Molland and S. R. Turnock, Marine Rudders, Hydrofoils and Control Surfaces: Principles, Data, Design and Applications (Butterworth-Heinemann, 2021).
- 44Y. Zhang, Influence of Drift Angle on the Self-Propelled Ship's Powering Performance in Waves (University of Southampton, 2023).
- <sup>45</sup>A. Claughton, "Developments in the IMS VPP formulations," in *SNAME* Chesapeake Sailing Yacht Symposium (SNAME, 1999), p. D021S002R001.
- 46 A. R. Claughton, J. F. Wellicome, and R. Shenoi, Sailing Yacht Design: Practice (University of Southampton, 2006).
- <sup>47</sup>C. Böhm, "A velocity prediction procedure for sailing yachts with a hydrodynamic model based on integrated fully coupled RANSE-free-surface

- simulations," Doctoral Thesis (2014); available at https://repository.tudelft.nl/ record/uuid:27c98a96-8b2e-4797-a9ea-76f5f5cbab48#title.
- 48 J. Hou, G. Liu, Q. Tan, K. P. Mok, W. Song, K. Y. Chan, R. C.-H. So, P. Zhou, and X. Zhang, "Velocity prediction program for windsurfing: A hierarchical approach integrating biomechanical insights," Ocean Eng. 312, 119070
- <sup>49</sup>ITTC, Recommended Procedures and Guidelines: Testing and Extrapolation Methods-Propulsion, Performance Propulsion Test (ITTC, 2008).
- <sup>50</sup>A. Molland and S. Turnock, "Wind tunnel investigation of the influence of propeller loading on ship rudder performance," Ship Science Report No. 46 (University of Southampton, 1991).
- $^{\bf 51}{\rm J.}$  Gerritsma, J. A. Keuning, and A. Versluis, "Sailing yacht performance in calm water and in waves," in SNAME Chesapeake Sailing Yacht Symposium (SNAME, 1993), p. D011S001R001.
- 52N. J. van der Kolk, I. Akkerman, J. Keuning, and R. Huijsmans, "Low-aspect ratio appendages for wind-assisted ships," J. Mar. Sci. Technol. 26, 1126 (2021).
- $^{53}\mathrm{M}.$  M. Munk, "Remarks on the pressure distribution over the surface of an ellipsoid, moving translationally through a perfect fluid," Report No. NACA-TN-196 (National Advisory Committee for Aeronautics, 1924).
- <sup>54</sup>K. Kume, J. Hasegawa, Y. Tsukada, J. Fujisawa, R. Fukasawa, and M. Hinatsu, "Measurements of hydrodynamic forces, surface pressure, and wake for obliquely towed tanker model and uncertainty analysis for CFD validation," J. Mar. Sci. Technol. 11, 65 (2006).
- 55J. V. Kramer and S. Steen, "Sail-induced resistance on a wind-powered cargo ship," Ocean Eng. 261, 111688 (2022).
- <sup>56</sup>S. Hosseinzadeh, S. Turnock, H. Lee, and R. Olvera (2024). "Dataset in support of the paper 'Experimental dataset of a model-scale ship in calm water and waves,' Dataset, University of Southampton. https://doi.org/10.5258/SOTON/D3076
- 57G. Farnebäck, "Two-frame motion estimation based on polynomial expansion," in Scandinavian Conference on Image Analysis (Springer Berlin Heidelberg, Berlin, Heidelberg, 2003), pp. 363-370.